

Electrical Characterisation of (Ag,Cu)(In,Ga)Se₂ Thin Film Solar Cells To Investigate Stability

Patrick Pearson

Abstract

This licentiate thesis gives a summary of electrical characterisation techniques, detailing their use to investigate and understand stability and meta-stability in thin-film solar cells, with a focus on the chalcopyrite material system. Experimental data is used to illustrate the information that can be extracted with these measurements, highlighting the deeper insights that can be drawn from complementary measurements. For example, short-circuit current losses in (Ag,Cu)(In,Ga)Se₂ after prolonged storage and annealing are attributed to changes in the net doping, as are significant open-circuit voltage losses observed after lightsoaking. Characterisation is also shown to suggest that the amount of Ag in the alloy plays a significant role in its stability, with a similar significance indicated for Ga.

Contents

1	Introduction	3
1.1	Aim of the Thesis	4
1.2	The Chalcopyrite Material System	4
1.3	Stability and Meta-Stability in Cu(In,Ga)Se ₂	6
2	Current-Voltage and External Quantum Efficiency Measurements	11
2.1	Current-Voltage Measurements	11
2.2	External Quantum Efficiency Measurements	14
3	Capacitance-Based Measurements	16
3.1	Capacitance-Voltage Measurements	17
3.2	Admittance Measurements	20
4	Research Highlights	26
4.1	Experimental Details	26
4.2	Paper One - Long Term Stability of CIGS and Kesterites After Irradiation	27
4.3	Paper Two - Stoichiometry and ACIGS	27
4.4	Paper Three - Ag and Ga Impact on ACIGS	33
5	Summary and Outlook	35
6	List of Papers	46

1 Introduction

It is well known that the world is in the midst of an environmental crisis and the window of time left in which to avoid a climate catastrophe is narrowing rapidly [1]. Perhaps the single most important task for society is to transition from a fossil-fuel driven energy network, to a predominantly electrified system powered by renewables. Solar energy is just one of a range of renewable power-generation solutions, however it is the one with the greatest potential and lowest costs [2, 3].

For the past thirty years thin film solar cells (TFSCs) have consistently held a market share of around 5 – 10%, with the remaining 90 – 95% dominated by silicon technologies [4]. Despite this, there has been significant interest surrounding, and research into, TFSC. This interest is rightly justified by the enhanced flexibility and reduced resource consumption of the technology. Due to high absorption coefficients and direct bandgaps, absorber layers in TFSC are in the order of several micrometres thick, compared to the several hundred micrometre thickness of Si absorber layers [5]. The reduced resource consumption of thinner absorber layers reduces the financial and energetic costs of production, the latter consideration being highly relevant, especially when it is considered that the majority of Si modules are manufactured in China, which relies heavily on coal for electricity production [6]. The reduced thickness and mass of TFSC allows devices to be produced that are literally and figuratively more flexible than their Si counterparts, with a wide range of processing methods open to use. TFSC can easily be used in building facades and incorporated into many everyday objects and are excellent candidates for use in space due to their low mass, pairing excellently with the rise in mini-satellites. Of course, typical rooftop and utility modules are also produced using TFSC, notably CdTe and Cu(In,Ga)Se₂ (CIGS). Thin film absorber materials are also commonly highly tunable, such that semi-transparent or coloured devices can be produced, making them desirable for building integration and incorporation in multi-junction devices. In addition to their wide range of applications and adaptability, TFSC are also reaching high power-conversion efficiencies (PCE/ η) bringing down electricity costs and making them a competitive choice (record CIGS cell and module PCE are 22.6 % and 19.2 % respectively, with 21.0 % and 19.5 % for CdTe cells and modules [7, 8]).

Conventional single-junction solar cells have bandgaps designed to deliver a good efficiency over the entire incoming solar spectrum, however are forced to compromise, being unable to absorb the lowest energy photons and wasting much of the energy of the most energetic photons, due to thermalisation losses. This limits single junction efficiency to ~ 33 % [9]. Multi-junction solar cells exploit multiple absorber layers with differing bandgaps in order to maximise the utilisation of incident light. The most researched structure is the tandem (two junction) cell, with the top cell having a wide bandgap and harvesting the more energetic photons, whilst the bottom cell has a narrower bandgap and harvests those photons with less energy, which are transmitted through the layer above.

Depending on the design of the device, optimum bandgaps are $0.8 - 1.2$ eV for the bottom cell and $1.4 - 2.1$ eV for the top cell, leading to maximum theoretical efficiencies of $\sim 46\%$ [10].

1.1 Aim of the Thesis

The aim of this thesis is to explore how electrical characterisation can be used to study the stability and meta-stability of CIGS and silver-containing CIGS (ACIGS) devices, beginning with a brief summary of the development of CIGS as an absorber in TFSC, and a discussion of the stability and meta-stability concerns for the material. This will be followed by sections detailing measurement theory and application. This section aims to explain what data can be extracted from measurements and how theoretical considerations can be used to direct them in such a way as to extract more detailed information, and to provide evidence for background mechanisms. The thesis will then use examples from my own work on CIGS, ACIGS and kesterite devices to highlight how complementary measurements can be employed together in order to begin unravelling complex problems. This section draws on two already published articles (attached at the end of the thesis) and a third work entering the manuscript stage. The primary motivation for the thesis is to summarise and condense the learning of the first half of my PhD project, and to indicate what problems I will investigate and attempt to clarify in the final two years of my research time.

1.2 The Chalcopyrite Material System

A typical CIGS solar cell comprises of a layered stack in the substrate configuration. The stack structure which we commonly work with is $\text{ZnO:Al/ZnO/CdS/CIGS/Mo/Soda-Lime Glass (SLG)}$. The Mo and window structure are deposited using sputtering, chemical bath deposition is used for the CdS, and the CIGS is deposited using co-evaporation, as described below. Electrons are collected at the front of the device, and holes at the rear.

Research into CIS-based solar cells began in the 1970s at Bell Laboratories [11] and expanded in the 1980s, along two routes - co-evaporation and deposition reaction from metal precursors. Initially the latter method gave better results, but in 1995 the important contribution of Na to device performance was discovered, as SLG became the standard glass used for substrates in devices produced via co-evaporation. A rapid catch-up of co-evaporation-processed device PCE to levels similar to those for devices produced from metal precursors followed [12]. Another major breakthrough in device design and performance was the development of the three-stage process at the National Renewable Energy Laboratory in 1994 [13]. This process employs an initial deposition of In, Ga and Se, followed by the deposition of Cu in a Se-rich atmosphere, and a final deposition of In, Ga and Se to return the absorber to a Cu-poor state. The α -phase region of CIGS is very narrow and deviation into the Cu-rich region of the phase

diagram leads to the formation of Cu_2Se which leads to high shunt conductivity in the absorber layer, hence the design of a process that ensures Cu-poor material [14, 15]. Moreover, Cu_2Se tends to segregate to the CIGS/CdS interface, affecting the junction properties and increasing local recombination such that it becomes a limiting factor in device performance [16, 17]. In contrast, the ordered-defect compounds found in the Cu-poor regime are relatively benign to device performance. Given the negative effects of Cu-rich material on device performance, it is worth explaining why the second stage of the process is included. Several benefits of Cu-rich growth have been observed, with the primary motivator of the inclusion of the Cu-rich growth stage being the promotion of large grain growth, and thus fewer potentially performance-reducing grain boundaries in the device [13]. The crystal quality, charge carrier mobility and diffusion lengths are also greater in Cu-rich material than in Cu-poor, however efforts to exploit these benefits and produce high quality devices have thus far failed [18].

The exact role of Na in CIGS is unknown, but there appear to be connections to doping, reducing compensation from In_{Cu} shallow donors [19]; a firm improvement of the rear contact (Na enhances the formation of MoSe_2 which is essential for an Ohmic contact [20]) and also passivation of the grain boundaries [21]. These processes are manifested in improvements in the open-circuit voltage (V_{OC}) and fill factor (FF). The inclusion of heavier alkali metals (Rb, Cs and K) has also led to significant gains in device performance, although all three alkali treatments are observed to have similar effects on devices. For devices with SLG substrates, Na diffuses into the absorber during processing. Alternatively, post-deposition treatments (PDT) utilising fluoride are also used to introduce alkali metals into CIGS devices, meaning that devices grown on alternative, perhaps transparent, substrates may also benefit. Precursor layers including alkalis may also be used, for example a NaF layer. KF PDT was observed to have the additional effect of altering the CdS-CIGS interface chemistry (it is claimed that Cu depletion occurs, allowing beneficial in-diffusion of Cd), such that a thinner CdS layer could be employed, reducing parasitic absorption of incident radiation [22]. It is otherwise observed that the beneficial effects of K are weaker than those of Na (rear-barrier removal and increase of the hole concentration). Interestingly, it seems that a KF PDT allows the incorporation of greater quantities of Na than if no K is present in the system. It is worth noting that due to inhomogenities in Na distribution in SLG, a Na-blocking layer is added in module production, and a uniform NaF layer deposited on top of the Mo during processing, such that a controlled amount of Na can diffuse into the CIGS layer [23].

Ga addition increases the bandgap of CIGS, primarily through increasing the energetic height of the conduction band [24]. Furthermore, the α -phase region of CIGS is widened through Ga addition, increasing the tolerance to off-stoichiometry [25]. Ga grading is commonly applied to CIGS absorber layers, such that the GGI ($[Ga] / ([Ga] + [In])$) increases towards the rear contact and

CIGS/CdS interface (notch profile). Ga grading at the rear of the cell serves to repel electrons, thus reducing recombination losses at the back contact. Likewise, an increase in the conduction band edge at the front interface advantageously increases the energetic separation to the valence band and defect levels in the mid-gap, reducing recombination. The GGI minimum corresponds to the bandgap minimum and of course represents a minimum of generation losses and thus should be located near the front surface. On the other hand, a reduced bandgap correlates to an increase in recombination, so the width of this notch should be constrained [26, 27]. In addition to Ga addition, substitution of Se with S also increases the bandgap, through reduction of the energetic height of the valence band maximum and an increase in the conduction band minimum [24]. Such a band alteration makes for a highly favourable interface, such that S-grading is sometimes used at the front surface of the CIGS layer [28]. There are, however, difficulties in controlling sulfurisation, using processes that avoid the highly hazardous H_2S gas.

It is desirable to fabricate wide-gap CIGS with bandgaps greater than the more commonly used 1.2 eV. There are a range of motivations for such a wide-gap absorber layer, namely reduced resistive losses in monolithic series-connected modules (due to higher voltages, lower currents) and the suitability for use in tandem devices as top cell. However it has been observed that in CIGS the increase in V_{OC} is not linear with bandgap, as one might expect [29, 30]. Instead it is seen that as GGI increases above an optimum of ~ 0.3 , device performance deteriorates, with primary reasons being: An increase in both the concentration and energetic depth of the Ga_{Cu} deep defect [31, 32]; an increasingly disadvantageous conduction band-offset (CBO) between the CIGS and CdS [33, 34]; Cu-enrichment of grain boundaries, leading to worsening shunts and increased recombination [35, 36], and tetragonal distortion of the crystal lattice [37].

It is expected that the partial substitution of Cu with Ag could counteract some of the negative impacts of high GGI in CIGS: Improved CBO can be achieved through downshifting of both conduction and valence bands with increased silver content [38]; lower alloy melting temperatures lead to reduced formation of deep defects [39, 40], and an increase in grain size is also observed (reducing the impact of malign grain boundaries), enabling the use of transparent or flexible substrates with high quality absorber material [41, 42]. Indeed there have been many reports of high quality CIGS devices utilising Ag-substitution, for both narrow- and wide-gap absorbers, and on a range of substrates [43, 44, 45, 46].

1.3 Stability and Meta-Stability in $\text{Cu}(\text{In,Ga})\text{Se}_2$

When discussing stability, we must first differentiate between long-term stability and meta-stability. The first case has implications for the implementation and commercialisation of a photovoltaic material, relating to how prolonged exposure to voltage bias, illumination, atmospheric conditions and heat cycling effect performance, primarily the device efficiency. Meta-stability involves semi-

persistent states that can be induced through some perturbation of the system, shifting it into a local (but not global) energy minimum for example after light exposure, annealing or the application of a bias. Causes of long-term stability phenomena can be the directional migration of mobile species across the bulk, or oxidation/reaction with other atmospheric elements. Meta-stabilities can arise due to ion migration, but also due to modulation of carrier or defect concentration through the activation of some mechanism.

Concerns for long term stability of CIGS originate primarily from the high mobility of Cu and Na ions in the material [47, 48]. However the high mobility of Cu may also prove to be beneficial in this regard, as relaxation after stress is enhanced [48]. Ion migration is, of course, particularly enhanced by the application of bias. Indeed, Fjällström et al. saw that potential-induced degradation has a clear link to Na content. This degradation was, however, observed to be mostly reversible with considerable recovery after a six month storage period [47]. Furthermore, it has been observed through prolonged damp heat and illumination treatments, that Na migration and accumulation can lead to shunt and series resistance problems, with similar issues resulting from water ingress into the ZnO structure layer [49]. Interestingly, heat-light soaking (HLS) treatments seem to lead to considerable recovery of long term stability losses suffered by K-containing devices (V_{OC} and FF) [50]. In my own work, it has also been observed that CIGS will recover considerably from damaging proton irradiation after prolonged dark storage [51]. In general, CIGS can be considered to have good long-term stability, though complications may arise for alkali-containing devices [48, 49].

CIGS has been observed to exhibit several meta-stabilities, namely an increase in V_{OC} due to persistent photo-doping induced by lightsoaking (LS). Dark annealing (often performed at 85 °C) accelerates the relaxation of this effect [52]. In addition to the response to white LS effects, meta-stable responses to blue- and red-LS have been observed, indicating responses at the CdS-CIGS interface and in the CIGS bulk, respectively [53]. Blue-LS increases the device FF and decreases the junction capacitance, whilst red-LS leads to an increase in the net acceptor concentration in the quasi-neutral region (QNR), but also dark-light crossover and current-voltage curve 'kinking' indicating the presence of a transport barrier. It is quite likely that the white-LS effects are quite simply a combination of those for blue- and red-LS. HLS has also been shown to have significant impacts on CIGS device performance, however there are reports of both positive effects (V_{OC} and FF improvements) and negative effects (decreases in PCE and increases in recombination centre density). Tangara, et al. recently reported that net charge carrier density increases after HLS, but so too does interface recombination. The study also indicated that the effects of HLS depend on the choice of buffer layer and presence of alkali species in the device [54]. Exposure to forward bias has been seen to have similar effects to red-LS, whilst reverse bias increases the junction capacitance, but may also lead to a reduction in net carrier concentration in the QNR [55].

When investigating meta-stability, it is important to attempt to define a stable baseline state, i.e. the relaxed state of the material. For CIGS this can be achieved through dark storage, though typically a short dark anneal at relatively low temperatures (85 °C is used to ensure relaxation, as even the most persistent of effects should be reversed with the addition of this thermal energy) [56]. It has been observed that in CIGS the relaxation time of bias- and light-induced meta-stabilities is proportional to the length of time the treatment was applied [57]. To effectively probe meta-stable induced states, it is advisable to perform measurements at low temperature ($T < 150$ K) to 'freeze-in' metastabilities and retard relaxation.

Defect driven mechanisms are the most prominent for explaining meta-stabilities in CIGS. Defects distort the perfect periodicity of the crystal lattice and lead to potential fluctuations which affect carrier transport dynamics. Additionally, the energetic depth of defects will change how they influence charge carrier concentrations in the material: 'Shallow' defects with energies close to the band edges (< 100 meV) act as dopants, providing additional free carriers (holes for near-VBM defects, electrons for near-CBM defects) above their ionisation temperatures (typically ionisation is complete above 200 K). 'Deep' defects have energies in the mid-gap, far from the band edges and act as carrier traps and recombination centres. Examples of shallow defects in CIGS are V_{Cu} , which acts as the primary p-dopant, and the donor In_{Cu} which acts to compensate the majority p-doping [58]. The most prominent deep defect is the donor-defect Ga_{Cu} which can become highly problematic for devices with high Ga content ($GGI > 0.3$) [31]. Of those defects which act as charge carrier traps, there are some which may capture more than one carrier at a time, despite the enhanced Coulomb repulsion. Such a defect is known as a 'negative-U' centre, owing to the negative potential and energetic favourability of a second capture event [59]. Most carrier-trapping defects are 'positive-U', and capture a single carrier. Negative-U defects show strong lattice relaxation effects upon capture and emission of carriers, as restructuring is critical to the energetic favourability of multiple carrier occupancy. This restructuring can lead to significant barriers to charge state transitions. Typically the emission of one carrier from a negative-U defect is immediately followed by the emission of the second, resulting in large step-wise changes in properties when probing a material with non-negligible concentrations of such defects. An example of a possible negative-U defect in CIGS is the divacancy complex ($V_{Se} - V_{Cu}$) [60].

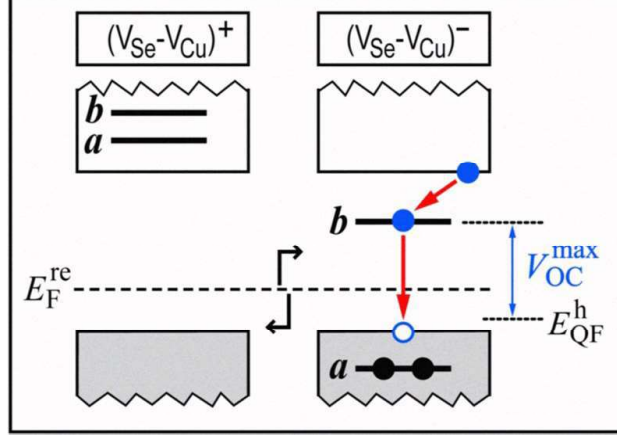


Figure 1: Schematic of the defect energies (a and b) of the $(V_{Se} - V_{Cu})$ divacancy complex in the acceptor (-) and donor (+) configurations, with relation to the CIGS band edges and Fermi level. In the donor configuration, both defects lie near the conduction band edge, acting as dopants, in the acceptor configuration one defect lies near the valence band edge (a), acting as a dopant. The second defect (b) in the acceptor configuration is in the mid-gap and acts as a deep defect, potentially limiting V_{OC} , as depicted. Taken from [61] Copyright © 2008, IEEE

The $(V_{Se} - V_{Cu})$ divacancy complex is also a primary contender to be the source of many of the meta-stabilities observed in CIGS, following a theory developed by Lany and Zunger [55]. This model suggests that the $(V_{Se} - V_{Cu})$ complex may occupy either an acceptor- or donor-type configuration, dependent on the position of the local Fermi-level (ϵ_F). The acceptor configuration consists of a paired shallow and deep acceptor level, the latter a single shallow donor level. Transitions between the acceptor and donor configurations are possible, and it is these transitions that lead to the persistent photo-conductivity and responses to blue- and red-LS, i.e. under white light bias, donor defects capture electrons and convert to the acceptor configuration after subsequent In-In bond contraction, increasing the net p-doping. More demanding conditions for acceptor-to-donor configuration transitions (greater energy barrier and the capture of two holes, as opposed to a single electron) suppresses relaxation to the initial configuration distribution, leading to a meta-stable state [55]. There are many experimental papers investigating meta-stability that yield results consistent with the Lany-Zunger model for CIGS [57, 60, 62, 63] and ACIGS [29, 64, 65]. An experimental indicator that such a defect reconfiguration, rather than a typical, positive-U deep defect capture/emission process is occurring, is that the relaxation rates after a negative or positive bias pulse are very similar. Typically for a deep defect, it is seen that capture rates far exceed emission [57].

Another type of defect involved in lattice restructuring is a DX centre. A DX centre is a strongly localised electronic state within the bandgap. When carriers are captured, it may become energetically favourable for the occupied defect to relax from the lattice site it occupies. Upon relaxation, the emission probability of the captured carriers shrinks, thus trapping them. It has been suggested that ionised In/Ga_{Cu} defects in CIGS may act as such DX centres, relaxing from the lattice and forming a complex of 2V_{Cu}-In/Ga_i²⁺ [66]. High densities of DX centres can lead to ϵ_F -pinning and, therefore, limit the V_{OC} . For example, the 2V_{Cu}-In/Ga_i²⁺ complex is initially self-compensating and charge-neutral. However as ϵ_F rises during perturbation, electrons may become trapped and lattice relaxation occur, leading to net negative complex formation, pinning ϵ_F . Meta-stabilities in doping and deep level capacitance response could be observed as a result of DX centres in a device. In the absence of free holes that might recombine with electrons trapped in the DX centres, carrier emission and return to the lattice would be a slow process due to the need to overcome the activation barrier. Thus at low temperatures, a persistent response to perturbation that can rapidly be dispelled through the application of reverse bias or blue-LS should be observed [66, 67].

Investigations into ACIGS with low Ag content and moderate Ga ($AAC \leq 0.25$, $GGI \leq 0.40$) have indicated stability results similar to that of Ag-free CIGS, both with regards to long-term stability, and heat- and light-induced meta-stabilities. In my previous and current works, the stability of high-Ga, high-Ag ACIGS was investigated ($0.45 \leq AAC \leq 0.65$, $0.71 \leq GGI \leq 0.77$), considering both the long term and meta-stable aspects, through combination of dark storage, dark annealing and LS treatments [68]. The first of these studies, investigated the effect of I/III stoichiometry on the stability of devices with $AAC \approx 0.60$ and $GGI \approx 0.75$, revealing a complex relationship between stoichiometry, doping and meta-stable phenomena in the devices, as well as serious potential concerns for long-term stability. It was observed that prolonged dark storage and annealing lead to an increase in net doping, whilst a short anneal and white LS led to the reverse. Low diffusion lengths in the material lead to depletion-dependent charge carrier collection, and subsequent large current gains(losses) for doping decreases(increases). Ongoing investigations indicate that the stability improves for a reduced Ag content ($AAC < 0.50$) and that Ga also plays a significant role in the (meta)-stability of ACIGS, with significantly different trends and treatment responses for the two ACIGS sample sets and a third set of Ga-free ACIS samples.

2 Current-Voltage and External Quantum Efficiency Measurements

Individual current density-voltage (JV) and external quantum efficiency (EQE) measurements can yield a wealth of information on solar cell performance, but they are also complementary techniques, coming together to provide a much richer understanding of cell behaviours. The two measurements will be described individually below and examples of their use together will be presented in the research highlights section.

2.1 Current-Voltage Measurements

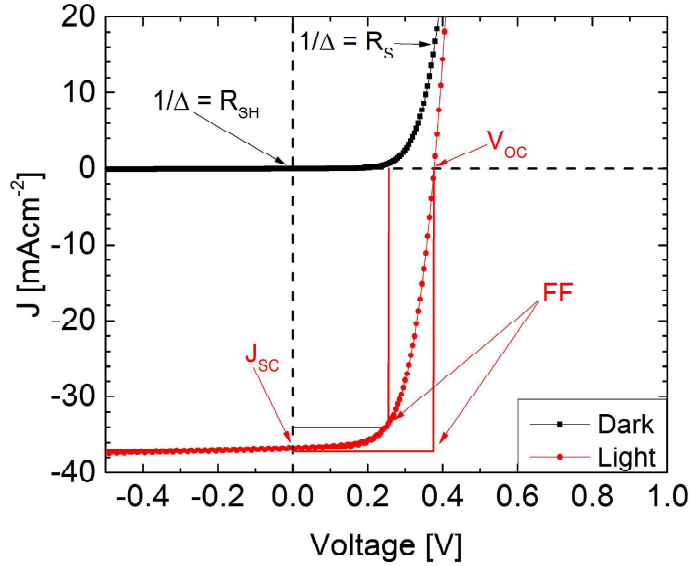


Figure 2: Dark and light JV curves indicating how estimates of key parameters can be easily extracted. V_{OC} and J_{SC} may simply be read from the axes; the resistances are the inverse gradients at the respective locations, and FF is the ratio between the actual maximum power, and that which could be achieved if V_{OC} and J_{SC} could operate simultaneously.

JV measurements are one of, if not the most, common techniques of solar cell analysis and can provide important information on the solar cell performance at a glance. Moreover, with variation of temperature, or application of light bias and/or voltage bias, an even richer cache of data is open to explore. To understand what parameters we may extract from JV measurements, we must

first introduce the basic equations governing current flow through a (photo)-diode:

$$J = J_0 \left[e^{q(V-JR_S)/nk_BT} - 1 \right] + \frac{V - JR_S}{R_{SH}} (-J_L) \quad (1)$$

Where n is the diode ideality factor; R_S is the series resistance (defines the slope at switch-on); R_{SH} is the shunt resistance (defines the slope around zero bias); J_L is the photo-current density (often assumed to equal the short-circuit current density J_{SC}), and J_0 is the reverse dark current density, given by:

$$J_0 = J_{00} e^{-E_A/nk_BT} \quad (2)$$

Where J_{00} is a temperature-independent factor, E_A the dominant recombination activation energy, k the Boltzmann constant, and T the temperature. Although there are arguments supporting the use of a two-diode model, for example if there is 'kinking' or rollover in the JV curve, indicating a charge transport barrier, it is typical to use the one-diode equations presented above. Data analysis and parameter extraction typically follows the procedure described by Hegedus et al., which allows for the removal of parasitic resistance contributions and aids in checking whether or not the device under test is 'well-behaved' and thus well approximated by the one-diode model assumptions [69]. Parameters can also be quickly estimated by inspection, as shown in fig.2, although series-correction is not included and there can be ambiguity in plotting fit lines to extract resistances.

For low shunt conductance ($G_{SH} \ll J_{SC}/V_{OC}$) the V_{OC} can be defined as:

$$V_{OC} \approx \frac{E_A}{q} - \frac{nk_BT}{q} \ln \left(\frac{J_{00}}{J_L} \right) \quad (3)$$

Thus, it can be seen how a plot of V_{OC} against temperature can yield the activation energy of the dominant recombination mechanism in the device, J_{00} and n . Linear fitting and extraction is performed in the region where it is assumed that n is independent of temperature. If $E_A < E_G$ there is a strong indication that interface recombination is the dominant recombination process. Otherwise, it is assumed that the majority of recombination occurs in the QNR or space-charge region.

Voltage Dependent Collection:

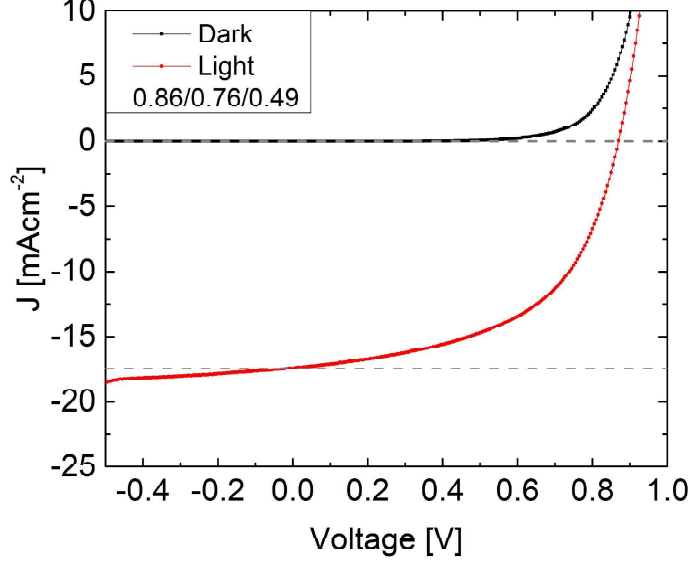


Figure 3: A comparison of the light- and dark-JV curves for an ACIGS sample. This sample is clearly exhibiting voltage-dependent collection, as seen by the differing dark- and light-shunt slopes. **Note:** The legend 0.XX/0.YY/0.ZZ denotes the composition - (I/III)/G/GI/AAC

The simple assumption that the photo-current is constant and equal to J_{SC} is rarely correct, however it is often not a huge source of error. In some devices, however, voltage-dependent collection ($\eta_C(V)$) plays a significant role. The most common example of a device with non-negligible $\eta_C(V)$ is one with an extremely low diffusion length, such that carrier collection is near-zero outside of the depletion region. The easiest way to evaluate the magnitude of voltage-dependent collection is to observe the apparent shunt slope of the device under illumination. Ideally the illuminated and dark shunt slope should be equal, but an increase in apparent shunting under illumination is due to $\eta_C(V)$. In some cases, a device with no clear slope in the dark may appear significantly shunted under illumination, indicating that there are considerable collection problems in the device (fig.3). It is assumed that the measured photo-current of a device is given by:

$$J_L(V) = \eta_C(V) * J_{L0} \quad (4)$$

Where J_{L0} is the maximum photo-current that would be achieved, assuming perfect collection. There are multiple models defining $\eta_C(V)$, each with a different set of assumptions [70]. In the case of perfect collection in the depletion region and for all carriers generated within one diffusion length, $\eta_C(V)$ is given

by:

$$\eta_C(V) = 1 - e^{-\alpha(\lambda)W(V)} (\alpha(\lambda)L + 1)^{-1} \quad (5)$$

Where $\alpha(\lambda)$ is the absorption coefficient of the absorber layer, $W(V)$, the depletion width, and L the minority carrier diffusion length.

2.2 External Quantum Efficiency Measurements

In the very simplest of terms, EQE is the ratio of electrons extracted from a device to photons incident upon it. The resulting efficiency is a combination of absorption and collection properties. In some cases, e.g. for incoming photons with energies below the bandgap, it is clear to separate these contributions (zero absorption in this case), however it is not always trivial to do so. Through integrating the measured EQE with the *AM1.5* spectrum, the J_{SC} of a device can be calculated:

$$J_{SC} = q \int_0^\infty EQE(\lambda) \phi(\lambda) d\lambda \quad (6)$$

Where q is the electron charge and ϕ the photon flux. Through analysis of the long-wavelength cutoff (absorption edge) the bandgap can be extracted. A connection to absorption depth can be made through consideration of the wavelength (energy) dependence of the signal, enabling a qualitative analysis of losses within the device.

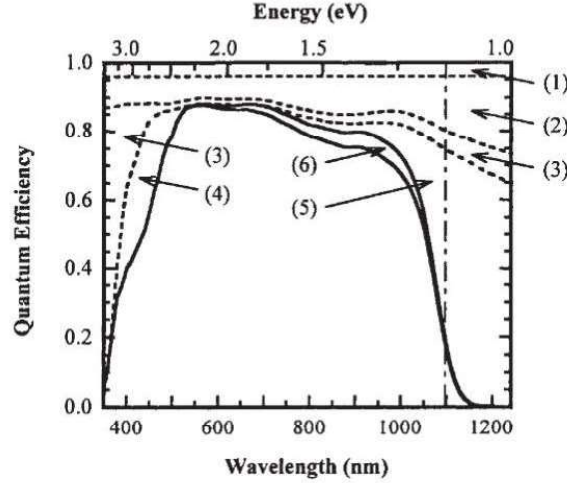


Figure 4: Diagram indicating from which portions of an EQE curve inferences on losses can be made. (1) indicates grid losses; (2) reflection; (3) TCO absorption; (4) buffer absorption; (5) incomplete absorption; (6) incomplete collection. Taken from [69] Copyright 2004 John Wiley & Sons, Ltd.

Loss analysis of EQE spectra (fig.4) gives information primarily on optical losses: parasitic absorption in the TCO, both at low wavelengths due to band-to-band transitions, and at long wavelengths due to free carrier absorption; parasitic absorption in the CdS buffer layer, due to band-to-band transitions; reflection from the top surface and interface scattering (combined due to complexity); incomplete absorption near the band edge. Incomplete collection due to recombination in the device can also be observed in EQE spectra. Typically this manifests as an early decline from peak plateau to the band edge, indicating bulk recombination as the dominant factor, however a wavelength independent reduction in EQE can be indicative of interface recombination. By applying a negative bias to the cell during EQE measurements, bulk recombination effects can be largely removed, through expanding the depletion region (with the assumption that there is near perfect collection in the depletion region). Conversely, the application of a forward bias allows an evaluation of how depletion dependent the charge carrier collection is in the cell (fig.5). An effective technique is to compare the ratios of EQE with and without bias, as a function of wavelength. For a flat signal, i.e. limited bias influence, the loss mechanisms effecting carrier collection are wavelength independent, e.g. interface recombination, additional transport barriers or series resistance. Such measurements can be combined with η_C (V) considerations discussed in section 2.1.

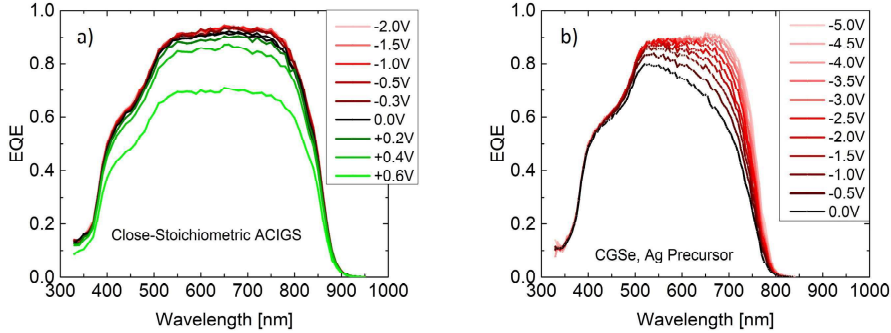


Figure 5: Voltage biased EQE measurements for a fully-depleted ACIGS device (a) and a highly doped CGSe device with Ag precursor layers (b). For the fully depleted device, reverse bias brings minimal gains, but for the highly doped device, a strong improvement is observed.

It is important to note that in some cases carrier collection may have a wavelength or intensity dependence, leading to the case where $J_{SC,EQE} \neq J_{SC,JV}$ [69]. The implementation of light bias during EQE measurements can assist in detecting such properties. If such concerns are present, a good procedure would be to perform EQE measurements once without bias and once with white light bias. If significant discrepancies are observed, further measurements with blue-

and red light bias can reveal more information. This procedure is also beneficial to probe trapping and photoconductivity in the device being tested. These effects can lead to changes in the space-charge region, leading to depletion width variations, which in turn affect charge carrier collection, depending on the minority carrier diffusion length. Such meta-stabilities would also be observed under red- or blue LS during JV measurements, as discussed in subsection 1.3.

3 Capacitance-Based Measurements

As described in sections 1.2 and 1.3, defects play an important role in the performance and stability of CIGS devices, providing p-type conductivity and also causing meta-stabilities and recombination. In order to gain deeper understanding of device performance and efficiency losses, it is desirable that the doping characteristics (depth profiles, concentrations, charge type) of absorber layers can be investigated. Capacitance-based techniques provide an intuitive way to gain insight, though data interpretation can be far from trivial, leading to a range of techniques developed to separate real phenomena from measurement artifacts and noise.

The most basic capacitance techniques are capacitance-voltage profiling (CV) and capacitance-frequency profiling (admittance measurements), which will be discussed in detail below. Both techniques make use of several common assumptions, namely that the junction is one-sided due to highly asymmetric doping levels in the p- and n-layers (n^+p in the case of the CdS-CIGS junction) and that the depletion region can be modelled as a parallel plate capacitor.

Typically, the slope of the 'Mott-Schottky' plot of $C^{-2}(V)$ is used to extract the net shallow doping in a device, whilst steps in admittance spectra are used to identify deeper defects. Due to the layered stack nature of TFSC, several assumptions must be made (primarily leading to the conclusion that only the absorber layer contributes to measurements), but there is still some uncertainty in the quality and interpretation of the data. Identifying trends, rather than exact values, should be the goal of such measurements. Interdiffusion across interfaces can lead to compositionally graded transition regions (which could, for example, effect the validity of the abrupt single sided junction approximation). Other electronic effects may cause steps in admittance spectra, such as transport phenomena, interface barriers or layer structure effects. Moreover, a given step may have multiple causes that cannot be individually resolved. It has been suggested that to distinguish between defect origins and interface or transport steps, PL can be used in concert with admittance measurements, in addition to applying forward and reverse bias during the latter. To develop a full understanding, a more comprehensive investigation using temperature- and voltage-dependent capacitance and JV measurements would be required, in addition to Hall measurements [71].

3.1 Capacitance-Voltage Measurements

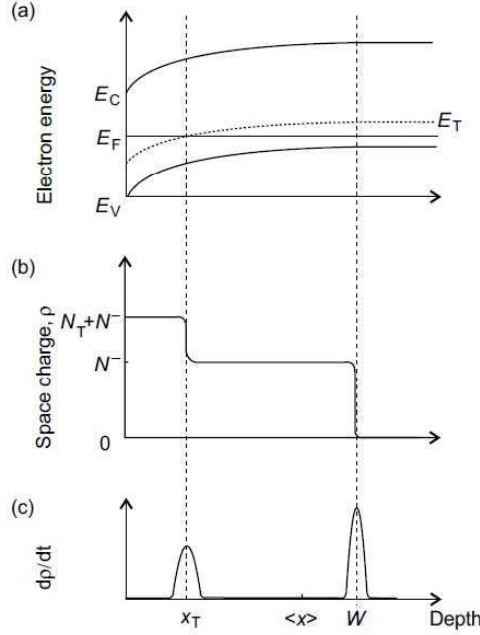


Figure 6: An energy band diagram (a) including a trap level E_T which changes occupancy upon crossing E_F , leading to a change in the space charge (b) at the crossing point (demarcation length). An applied bias will modulate the space charge at both the demarcation length and depletion edge (c). Taken from [72] Copyright © 2011 Wiley-VCH Verlag GmbH & Co. KGaA

CV profiling is performed through the application of a small oscillating voltage δV with frequency f_{CV} , in tandem with an applied bias V_{DC} . δV perturbs the occupancy of defect states close to the depletion edge, giving rise to a change in charge δQ , in turn leading to a capacitance $C = \frac{\delta Q}{\delta V}$. Trap state occupancy may also be perturbed away from the depletion edge, due to potential-induced fluctuation in E_F (fig.6). Through the measurement of changes to a signal current, C can be deduced. V_{DC} applied in the reverse (forward) direction acts to expand (contract) the depletion region, through application of a parallel (anti-parallel) electric field. In this way, a depth profile can be extracted for the net doping and capacitance response, as V_{DC} is varied. The capacitance is defined as:

$$C = A \sqrt{\frac{q\epsilon_0\epsilon_r N_{net}}{2(V_{bi} - V_{DC})}} \quad (7)$$

Where V_{bi} is the built-in potential, which in theory can be extracted from the Mott-Schottky V-axis intercept, but in reality is highly ambiguous to extract. N_{net} is the net dopant density (acceptors in the case of CIGS). Rearranging to find N_{net} returns:

$$N_{net} = \frac{-2}{q\epsilon_0\epsilon_r A^2} \left(\frac{d[C^{-2}]}{dV_{DC}} \right)^{-1} \quad (8)$$

With a corresponding depletion width:

$$W = \sqrt{\frac{2\epsilon_0\epsilon_r (V_{bi} - V_{DC} - 2k_B T q^{-1})}{qN_B}} \quad (9)$$

Where the factor $2k_B T q^{-1}$ is due to the majority charge carrier contribution to charge distribution that is frequently neglected [73]. N_B is the net doping of the lightly-doped side of the junction, it is assumed that $N_{net} \approx N_B$. However both this assumption, and the relation given for W only hold when $V_{DC} < V_{bi}$. The Debye length L_D defines the smearing of the depletion edge and thus defines the accuracy of W and the validity of our assumption that the response location probed by δV upon application of V_{DC} is equal to W [74]. L_D is given by:

$$L_D = \sqrt{\frac{\epsilon_0\epsilon_r k_B T}{q^2 N_B}} \quad (10)$$

For values of ϵ_r and N_{CV} commonly observed in our measurements on ACIGS, i.e. $\epsilon_r = 10$, $10^{15} < N_B < 10^{17} \text{ cm}^{-3}$, we return $12 < L_D < 120 \text{ nm}$ but typically consider $300 < W < 2000 \text{ nm}$, so can expect that the assumptions hold in our case (ACIGS has rather low doping, which ensures the validity of the single sided junction assumption).

There are several important considerations when choosing measurement parameters for a CV measurement. Perhaps the most important is the sweep frequency, as this determines which trap states may respond to δV . Trap states have capture and emission times dependent on their energetic depth and the system temperature. If the measurement frequency exceeds the trap response frequency ($2\pi f_{CV} > \omega_T$) then the perturbation of the depletion edge is too rapid for the trap to respond, carrier capture/emission are not induced and the trap charge state is unchanged, meaning it does not contribute to C . Fig.7 illustrates this clearly, showing a clear decrease in N_{CV} as f_{CV} increases, indicating that an increasing fraction of trap states are unable to respond within the perturbation period. For f_{CV} of 1 MHz, the device is almost fully depleted. In order to identify an appropriate f_{CV} , an admittance measurement can be performed. f_{CV} should not be in proximity to a capacitance step observed in admittance and should coincide with phase angles (ϕ) approaching 90° . Measurements conducted with $\phi \leq 20^\circ$ have been seen to be unreliable [75]. High frequency measurements ($f > 1 \text{ MHz}$) can lead to inductive circuits and unreliable data,

e.g. negative capacitance values. For CIGS, $f_{CV} \sim 50$ kHz is considered reasonable [75]. In my measurements on ACIGS, I typically use $f = 60$ kHz as the 90° condition is met for frequencies centring on $f = 60$ kHz and no nearby step in admittance is observed.

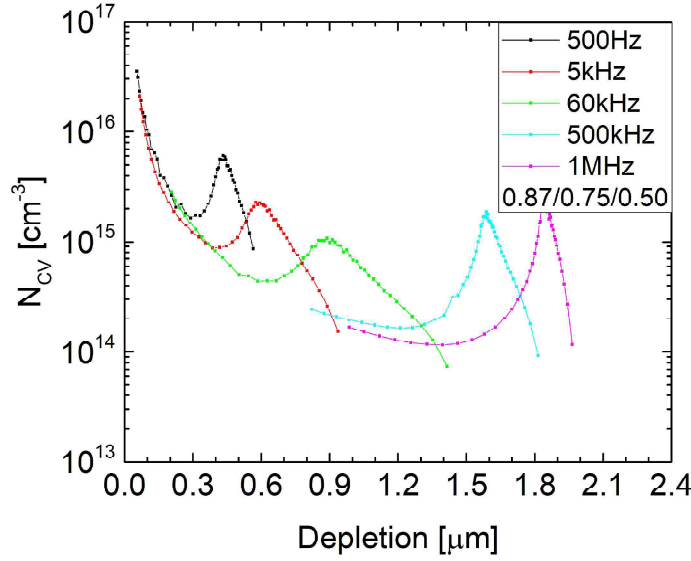


Figure 7: A comparison of the N_{CV} profile for the same ACIGS sample for a range of f_{CV} spanning from 500 Hz to 1 MHz and a voltage range $-0.5 < V_{DC} < 0.7$ V. As expected, increased f_{CV} leads to a reduced apparent N_{CV} and the typical CIGS 'u' profile is observed, with an additional tail. It can also be seen that the profiles converge for high forward bias. Reworked from Paper Two.

A second important sweep parameter is the sweep speed and the duration for which each bias is applied. Even if states cannot respond to δV ($\tau_T < 2\pi f_{CV}$) they can still contribute to the measured capacitance due to their existing charge state, which affects the band-bending. Thus there is a deep state contribution to CV measurements, so long as the trap energy E_T has time to equilibrate with the quasi- ϵ_F modulation and V_{DC} [71]. For long sweep durations ($t \gg \tau_T$) the defect charges equilibrate with V_{DC} and produce an electrostatic contribution to the capacitance. To account for this, measurements can be performed after holding the device under bias for several minutes, to achieve a determined base state. Switching from the defined bias to the desired V_{DC} gives an instant capacitance step (no deep defect contribution), followed by a relaxation to the steady state, including deep trap contributions. This is the basis of deep-level transient spectroscopy (DLTS). Alternatively, the sweep can be performed very quickly

($t < \tau_T$) such that the deep state charge does not change over the duration of the measurement. Through the comparison of measurements excluding the deep electrostatic contribution and those performed without taking additional measures, an understanding of the deep state density can be gained. Fast CV gives the physical net doping (traps don't change state) and bias-defined flat band state achieved by forward bias should ensure that all traps are full/empty (depends on species). If the deep states are in equilibrium with V_{DC} , the measurement gives $N_{CV} = N_A + N_T$ if ($\omega < \omega_T$) or $N_A < N_{CV} < N_A + N_T$ if ($\omega > \omega_T$) [76]. For significant N_T CV measurements will neither yield a clear indication of N_A , N_T , nor their uniformity if the preventative measures detailed above are not taken. The deep trap response has also been linked to strong hysteresis in CV measurements, which can be reduced either by utilising the fast CV method, or by performing measurements at low temperature (increasing ω_T) [77]. Low temperature measurements also serve to limit the effects of high bias, such that the first measurements in a CV sweep do not effect the subsequent measurements [78].

The third parameter for consideration is the applied voltage V_{DC} . It is important that $V_{DC} < V_{OC}$ in order to avoid excessive current flow [79]. Moreover, for long measurement durations, holding the device at high bias can damage or destroy the sample. Furthermore, it has been seen that the shape of the high forward bias regime of N_{CV} profiles is seemingly universal between samples of different material and quality, indicating a measurement effect, as opposed to a capacitance signal originating from the doping. This phenomenon can be observed in fig.7 and is suspected to relate to injection capacitance, see the comment of Ravishankar, et al. [80]. The perturbation voltage δV should also be small ($\delta V \ll V_{DC}$, $\sim 15mV$) in order to only modulate the very edge of the depletion region and reduce the overlap between adjacent measurement points.

3.2 Admittance Measurements

In a similar fashion to CV measurements, a small oscillating voltage (δV) is applied to the sample in admittance measurements. There is typically no bias voltage V_{DC} , instead the sweep frequency f is varied such that trap state contributions are gradually excluded from the measured capacitance, as $2\pi f > \omega_T$. The complex admittance, the inverse of complex impedance, is defined as:

$$Y(\omega) = \frac{1}{Z(\omega)} = G(\omega) + i\omega C(\omega) \quad (11)$$

Such that the real component of the signal gives the conductance and the imaginary component gives the capacitance. A more complete model accounting for inductance can be written as:

$$Z(\omega) = \frac{1}{Y(\omega)} = R + i\omega L + \frac{r(i\omega C)^{-1}}{(r + i\omega C)} \quad (12)$$

Admittance measurements become very powerful when performed within a cryostat such that the temperature-dependent admittance spectra can be analysed. Trap energies can be extracted from such a measurement through analysis of capacitance steps and their dependence on temperature and f . Capacitance steps are observed due to large densities of charge contributors being excluded from measurements, e.g. crossing the temperature threshold for dopant ionisation or the passing of ω_T for a significant defect band. To observe defect steps in the depletion capacitance, E_T must cross ϵ_F and ω_T must be within the measurement range [71]. States with the same E_T may have different ω_T due to differences in capture/emission cross sections. At low temperatures and high f , the capacitance is reduced to the geometric value $C_{geo} = \epsilon_r \epsilon_0 A/W$ (freeze-out). Capacitance steps can also be produced through resistance contributions (as f approaches the MHz range) and other measurement artifacts. Typically a single step will dominate within a given range of frequency and temperature, though this may be composed of multiple smaller steps, smeared together (this is suspected for the so-called 'N1' signal which is commonly observed in CIGS devices, even those produced with different processing methods and with varying quality [71, 81, 82]). In order to effectively interpret and understand the results of admittance measurements, it can be useful to apply a light or voltage bias. Above all else, it is important to have a concrete understanding of the assumptions built into the measurement technique and the equivalent circuit theory which is often used to relate the measured signals to the devices we study.

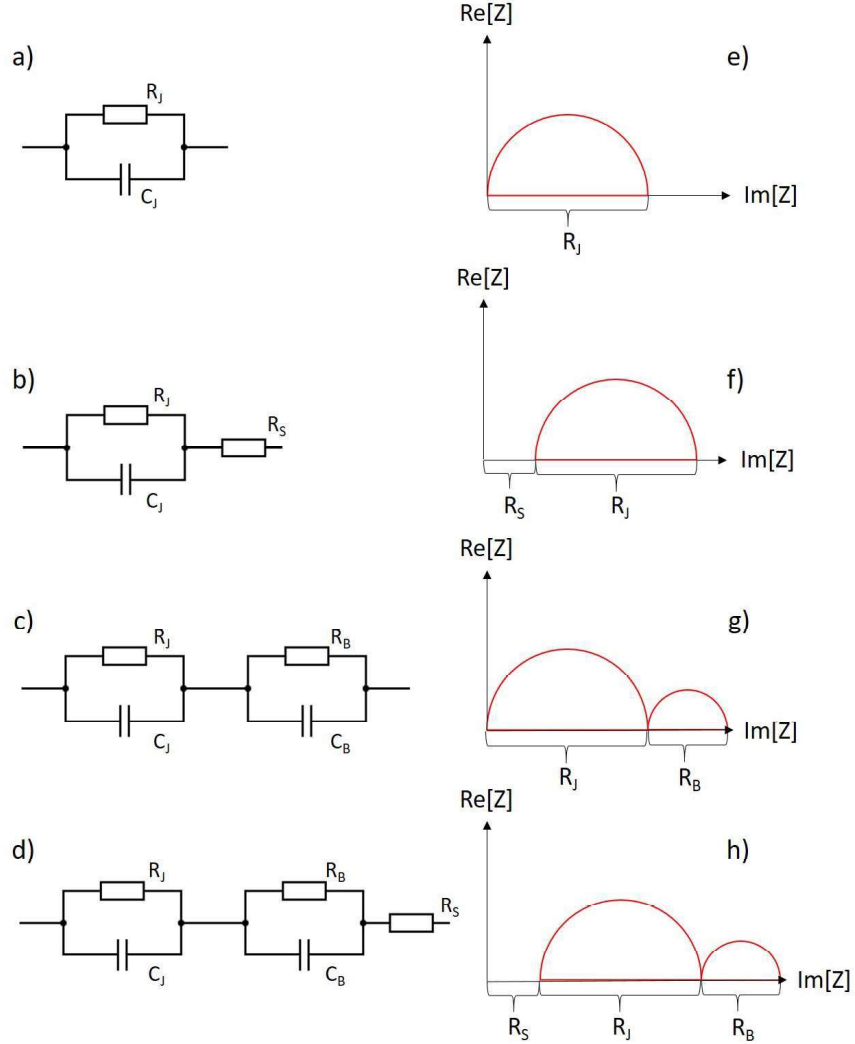


Figure 8: Equivalent circuits (a-d) with corresponding Nyquist plots (e-h). The circuits represent a single junction (a,e); a junction with non-negligible series resistance contributions (b,f); a junction with transport barrier (c,g) and a junction with a transport barrier and series resistance contributor (d,h).

The most basic equivalent circuit is the $C_P - R_P$ circuit consisting simply of a resistor and capacitor connected in parallel, representing the junction (fig.8.a). A common addition is a resistor in series (fig.8.b). A charge transport barrier, for example a second diode at the rear interface, can be modelled as an additional parallel connected resistor and capacitor, in series to the junction

component (fig.8.c). Constant phase elements (CPE) are somewhat artificial elements added to the equivalent circuit, replacing the junction capacitor and can represent many physical sources, for example spatial inhomogeneity (perhaps from grain boundaries) [83]. A CPE may be relevant to the equivalent circuit when the Nyquist plot has the shape of a circular arc, but not a true semi-circle centred on the $\text{Re}[Z]$ axis. An inductor may also be added to the circuit, accounting for measurement setup contributions (for example if using long wires), but also for high-frequency effects and physical phenomena. Sakakura, et al. suggested that an inductive loop in the Nyquist plot is due to inverse fields induced at the interface due to donors [84]. An effective way to evaluate how appropriate the equivalent circuit is, is to produce a 'Nyquist' plot, i.e. the real and imaginary components of the complex impedance. For a simple circuit consisting of just the junction component, the plot should be a perfect semi-circle (fig.8.e). Displacement along the $\text{Re}[Z]$ axis represents a series resistance contribution (fig.8.f). Additional semi-circles, or bumps can be due to additional barrier components (fig.8.g). A 'real' example of a Nyquist plot taken from an ACIGS sample is shown in fig.9 and indicates the inclusion of both a CPE, inductor and perhaps also a barrier element. As each component of the equivalent circuit has a physical origin within the device and a contribution to the impedance signal (due to the connection in series), the combination of measurement and equivalent circuit theory is powerful for the disentanglement of layer effects. However one must be cautious and refrain from relying too heavily upon such interpretations. Experience has shown that the Nyquist plot is extremely sensitive to contact quality, with even minor adjustments to the setup leading to significant shape changes and features. It is wise to compare the shape of the Nyquist plot to features observed in JV curves, as significant barrier or resistance contributions should be visible there too.

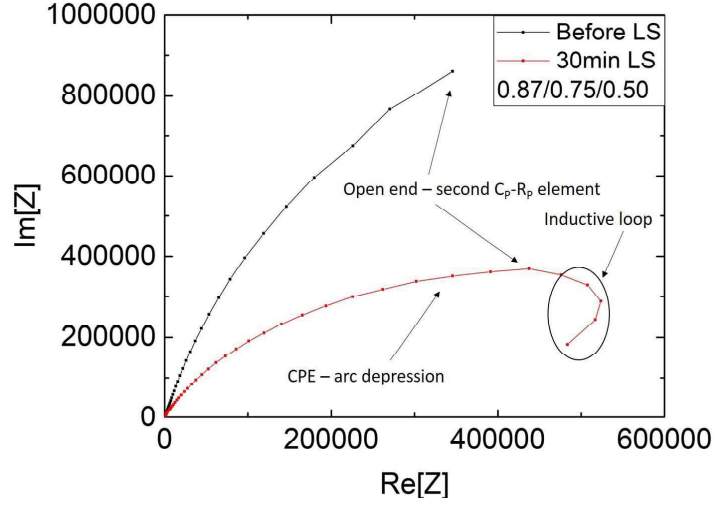


Figure 9: A Nyquist plot of an ACIGS sample before and after lightsoaking. Analysis of the shape suggests an equivalent circuit including a CPE, inductor and barrier element. This indicates that there are significant non-uniformities in the film and perhaps a defect rich interface.

In addition to considering the capacitance-frequency ($C(f)$) profile, one can consider the conductance-frequency ($G(f)$) profile (see fig.10). In this case, we do not see steps, but rather peaks. Peaks in $G(f)$ profiles are easier to discern than $C(f)$ steps, however they may overlap to an extent not seen in steps. Increased temperatures lead to $G(f)$ peaks shifting to higher f . Plotting the peak f against temperature by $\ln(\omega T^{-2})$ as a function of $1/T$, should yield a linear plot allowing extraction of E_T [85].

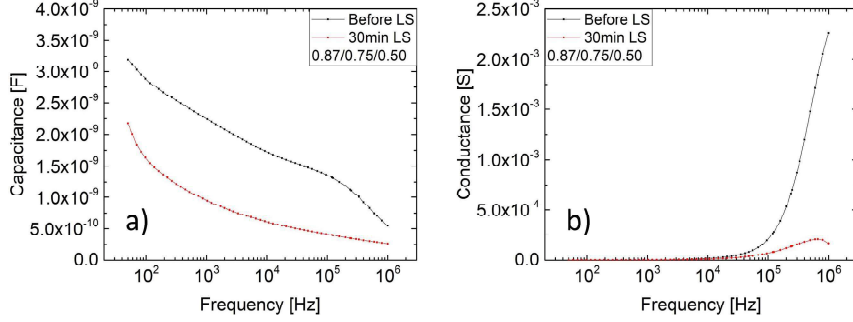


Figure 10: A comparison of the capacitance- and conductance frequency response measured at room temperature for the same ACIGS sample, before and after lightsoaking (a and b respectively). Note how the peak in conductance is easier to distinguish than the capacitance step. Reworked from Paper Two.

Considering the equivalent circuit comprising of standard $C_{B/J}$ - $R_{B/J}$ elements for the barrier and junction (as in fig.8.c), we yield the frequency response:

$$f_t(T) = \frac{1}{2\pi} \frac{G_B + G_J}{C_B + C_J} \approx \chi G_B(T) \quad (13)$$

Where χ is a constant. The simplification can be made due to the much higher conductivity of the barrier, in comparison to the junction. In the case where there is minimal, or no, barrier and capacitance steps are primarily caused by a defect the frequency response changes:

$$f_t(T) = \frac{1}{2\pi} V_{Th} N_{c,v} \sigma_{n,p} e^{-E_A/k_B T} \approx \chi T^2 e^{-E_A/k_B T} \quad (14)$$

Where V_{Th} is the thermal velocity, $N_{c,v}$ the density of conduction/valence band states, and $\sigma_{n,p}$ the capture cross-section of electrons/holes. Thus can temperature-dependent admittance spectroscopy assist in separating step causes.

By applying forward and reverse bias (V_{DC}) to the sample during admittance measurements, more insight can be gained into the origin of capacitance steps. If defect states are the origin of a step, then a response to bias should be expected due to shifting of the bands and ϵ_F relative to the trap level. If bias has no impact on the step, then it is indicative that the origin is a transport barrier within the device. For majority carrier traps, the quasi- ϵ_F which must be crossed is similar to the equilibrium level ($\epsilon_{Fp} \sim \epsilon_F$). However, for minority carrier traps there is an additional shift $\Delta\mu$ which has a voltage dependence, i.e. so too does the demarcation depth. Thus, the capacitance step height deriving from a majority carrier trap should be bias-independent (though disappearing in the flat band condition), whilst the height of a step derived from a minority trap should be bias-dependent [71]. An additional advantage of applying V_{DC}

during admittance measurements is, as in CV measurements, the ability to vary the probing depth of the measurement, through modulation of the band-bending and, consequently, the demarcation length and response regime of ω_T . [79].

4 Research Highlights

4.1 Experimental Details

Prior to discussing examples of experimental work, it is important to quickly outline some key details, namely the equipment used and the typical sample layout. JV and EQE measurements were performed using home-built setups, the former uses an ELH lamp for illumination and a water-cooled peltier element to keep the cell temperatures at 25 °C. Simple mechanical contact is made between probes and sample contacts in JV and EQE measurements. CV and admittance measurements were performed with an Agilent 4284A Precision LCR Meter and Keithley 2401 Source Meter. The material permittivity of ACIGS was taken to be 10, and this value was used for ACIS samples too. A material permittivity of 13 was used for CIGS and CIS. During CV and admittance measurements, contact is made by soldering contact wires to the rear contact and by making mechanical contact between the top contact and a probe. Four-point measurement is used at all times.

Each ACIGS processing run involved four samples, placed such that there is a lateral I/III stoichiometry grading, due to the arrangement of the elemental sources. The I/III variation across the run is approximately 10 %, with much smaller variations in *GGI* and *AAC* ($\sim 3\%$ for each). In contrast, the ACIS samples were measured to have a very narrow spread in I/III (no variation when rounded to two significant figures). CIGS and CIS samples were measured to have a variation of $\sim 5\%$ in I/III within sample sets. For all samples, we aim to produce an absorber layer of $2\ \mu\text{m}$ though there is some variation in the range of $\pm 0.2\ \mu\text{m}$. Samples are typically cut into two pieces, with one undergoing scribing to isolate cells, and the other remaining as a reference piece, available for future measurements or comparisons. Scribed samples contain twenty-eight cells in four rows of seven, each with an area of $0.05\ \text{cm}^2$. Normally only fourteen cells are measured per sample, with the remainder serving as back-ups (which proved to be useful after repeated measurements led to contact damage on other cells). No metal grid is deposited on the front surface, instead the measurement probe makes direct contact with the TCO. The rear contact is made by scratching away the surface to the Mo, and soldering a layer of indium on top. There is no anti-reflective coating applied.

4.2 Paper One - Long Term Stability of CIGS and Kesterites After Irradiation

My first work utilising the measurements discussed in this thesis was an investigation into the long term stability and recovery of kesterite ($\text{Cu}_2(\text{Zn},\text{Sn})\text{Se}_4$, $\text{Cu}_2(\text{Zn},\text{Sn})(\text{S},\text{Se})_4$) and CIGS thin-film solar cells three years after irradiation with protons [51]. It is widely reported that kesterites and CIGS devices have a much higher resilience to irradiation than, for example, silicon solar cells [86], and there is also significant evidence of device recovery from damage incurred by irradiation [87]. The irradiation damage primarily manifests itself in V_{OC} losses due to the introduction of defects into the material which act as recombination centres and perhaps also compensate the majority doping. The self-recovery from this damage is tentatively attributed to the mobility of Cu ions in the material, and is observed to accelerate with mild annealing. JV and EQE measurements were used to evaluate the continued recovery of the devices, whilst CV measurements supported speculation that remaining V_{OC} losses for CIGS devices were likely due to a persisting increase in recombination centres, rather than compensation, as N_{CV} was not unusually low (capacitance measurements had not been performed on the samples prior- or immediately after irradiation, so a direct comparison could not be made). Such a conclusion was supported by consideration of the EQE spectra, which suffered losses in the longer wavelength regime after irradiation and had not fully recovered to the initial state for those devices still exhibiting V_{OC} losses after the three year storage period. Kesterite devices were observed to exhibit FF losses, attributed to ageing due to a similar loss for each sample, irrespective of irradiation fluence.

4.3 Paper Two - Stoichiometry and ACIGS

As detailed in section 1.2, the partial substitution of Cu with Ag in wide-gap CIGS devices is expected to be beneficial for device performance. Our group has investigated a wide range of sample compositions for high-Ga, high-Ag ACIGS devices and indeed observed high V_{OC} and promising PCE [38, 44]. One such study revealed a low tolerance of I/III off-stoichiometry in the wide-gap ACIGS devices. I/III stoichiometry refers to the ratio of group-I to group-III ions in the lattice, with respect to the ideal stable ratio indicated in the chemical formula of the $(\text{Ag},\text{Cu})(\text{In},\text{Ga})\text{Se}_2$ formula, i.e. a ratio of 1 : 1 : 2 for the group-I (Cu and Ag) to group-III (In and Ga) to chalcogen (Se). A I/III-stoichiometry of 1.0, therefore, indicates that there is a 1 : 1 ratio of Ag and Cu to In and Ga, with values below one 1.0 indicating a deficiency of Ag and Cu. It was shown that for high AAC there was significant formation of ordered-vacancy compounds (OVCs) as the composition became group-I poor. In addition to OVC compound formation, it was observed that after a prolonged dark storage some devices exhibited blocking behaviour in JV curves, indicating charge transport barrier formation and a potential stability issue [88]. Utilising the techniques discussed in this report, I investigated a small subset of the ACIGS samples

with a relatively small spread in GGI ($0.71 - 0.77$) and AAC ($0.54 - 0.63$), but a wide variation in I/III ($0.79 - 0.98$) in order to evaluate their stability and the effect of stoichiometry [68]. In addition to a simple dark storage period (four to six months) all devices were annealed at low temperatures (85°C) for one hour, in order to effectively accelerate ageing. The samples were then split into smaller subsets, one undergoing a second anneal of twenty-four hours, and the other undergoing a five-hour LS treatment under AM1.5 illumination.

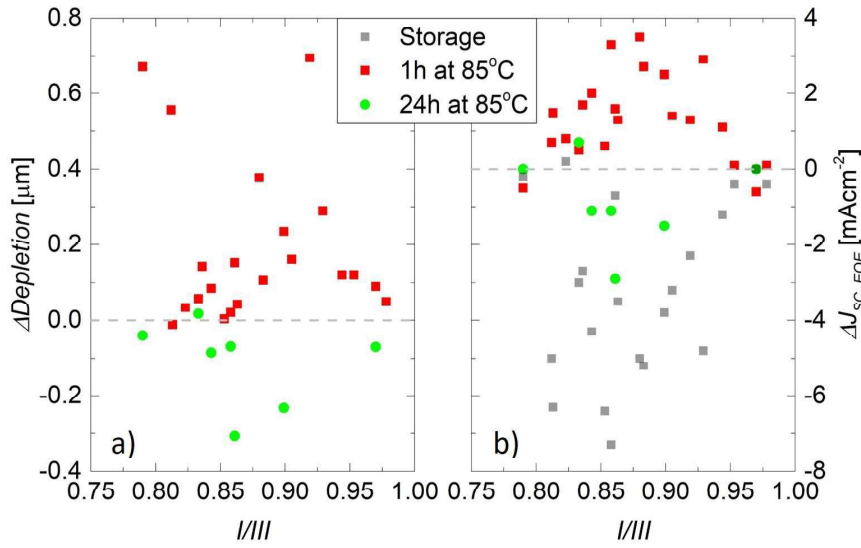


Figure 11: Variation in J_{SC} (a) and W (b) dependent on stoichiometry, as a response to annealing at 85°C for one- and twenty-four hours. The effect of prolonged dark storage on J_{SC} is also shown. A clear shared arch dependence is observed for both parameters. Reworked from Paper Two.

Initial analysis was performed using JV and EQE measurements, which revealed significant variations in J_{SC} after storage and annealing. Surprisingly, it was observed that the short, one hour anneal improved J_{SC} , whilst the dark storage and twenty-four hour anneal led to significant reductions (up to 40 % losses were observed after dark storage). This was unexpected, as at low heating temperatures it is expected that the main effect is that kinetic and statistical events are made more probable, i.e. time is accelerated and no additional mechanisms are triggered. A clear connection between stoichiometry and J_{SC} response was observed (fig.11). It was also observed that storage led to a decrease in V_{OC} and FF for close-stoichiometric devices, but annealing had no significant impact on these parameters. In an effort to understand the observed results capacitance measurements were performed on the samples. A clear dependence of N_{CV} on stoichiometry was observed (close- and extremely off-stoichiometric material

is almost fully depleted, moderately off-stoichiometric material in the region $0.82 < I/III < 0.92$ is highly doped) and variations in depletion width appeared to match those of J_{SC} very closely (fig.11). Equipped with this new knowledge of a causal connection between doping and J_{SC} , and an understanding of the dependence of doping on composition, we were able to begin trying to understand what was happening in the devices.

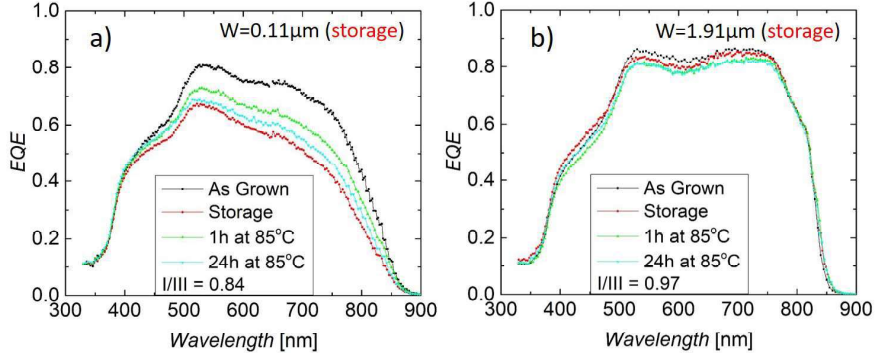


Figure 12: A comparison of the EQE spectra evolution for a highly-doped off-stoichiometric ACIGS device (a) and a near-fully depleted close-stoichiometric device (b) indicating heavy recombination losses and a greater response to treatment-induced doping changes for the former. Reworked from Paper Two.

By inspecting the shape of the EQE spectra for devices across the stoichiometric range, it was discovered that for the depleted material, the spectra were relatively square, but for highly doped samples, the more angular shape linked to high recombination losses was observed (fig.12). This observation, paired with the link of $W_{Dep} - J_{SC}$ led us to conclude that high-Ga, high-Ag ACIGS material has a very poor diffusion length, such that carrier collection is heavily depletion-dependent. We could also conclude that a time-dependent doping change was occurring in the material. The opposing direction of the short anneal doping change to the prolonged anneal and storage remained puzzling, but a possibility is that there are multiple mechanisms working in different directions and on different time scales.

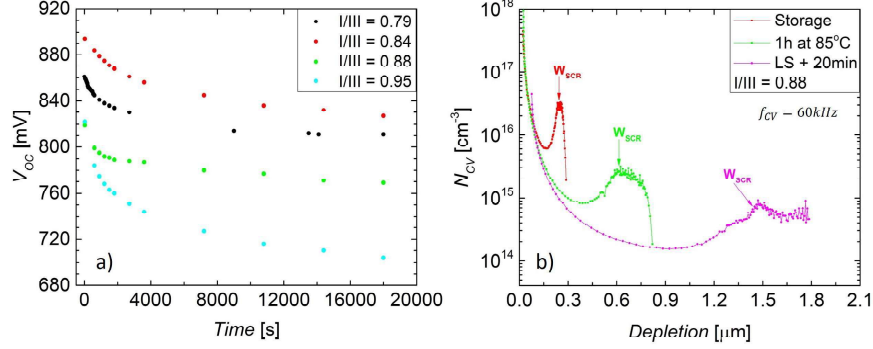


Figure 13: Time evolution of V_{OC} for high-Ga, high-Ag ACIGS samples under AM1.5 illumination (a) and the N_{CV} profile of one of the LS samples illustrating the change in net doping after LS (b). The V_{OC} degradation saturates at $t \approx 4000$ s, with remaining losses due to sample heating. The more off-stoichiometric the material, the less degradation is observed. Reworked from Paper Two.

The LS treatment also revealed interesting and unexpected results for JV parameters, namely a clear and significant decrease in V_{OC} with a strong dependence on stoichiometry (fig.13a). Capacitance measurements indicated a clear reduction in N_{CV} (fig.13b), proffering a simple explanation for the voltage loss. Based on literature observations for (A)CIGS (discussed in section 1.3) the expectation is for white-LS treatments to induce meta-stable increases in doping and V_{OC} , rather than the reductions I observed.

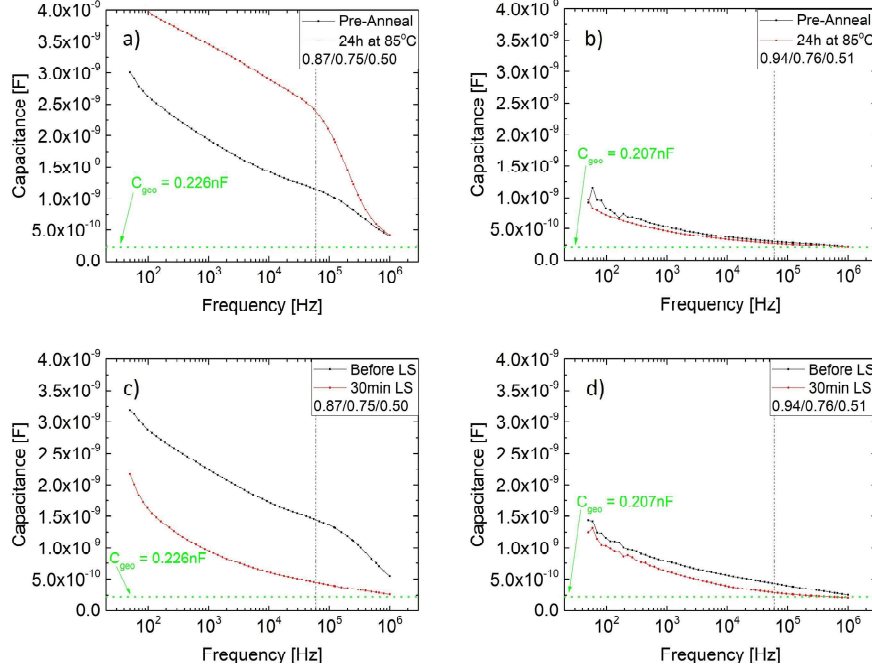


Figure 14: A comparison of the admittance spectra of high-Ga, high-Ag ACIGS before- and after a twenty-four hour anneal (a,b), and before- and after LS (c,d), for highly doped (a,c) and depleted (b,d) devices. The grey dashed line indicates the 60 kHz used for f_{CV} and the green dashed line represents C_{geo} . Reworked from Paper Two.

Admittance measurements were performed at room temperature, primarily to identify an appropriate measurement f_{CV} , but an insight can also be gained into the effect of treatments on the energetic landscape of the absorbers, as described in section 3.2. It can be clearly seen that depleted devices have a different $C(f)$ profile to the highly doped devices, and are also almost insensitive to treatments (fig.14b, fig.14d). The highly doped devices are observed to have a capacitance step around 100 kHz which is seemingly reduced by LS, but enhanced by annealing. Overall $C(f)$ follows the same behaviour. For our devices (thickness $\sim 2 \mu\text{m}$, area = 0.05 cm^2), it is estimated that $C_{Geo} \approx 0.22 \text{ nF} \approx 4.4 \text{ nF cm}^{-2}$, seemingly the value that $C(f)$ is converging upon after the step. This suggests that the step's origin is in the carrier freeze-out, as opposed to the crossing of a trap energy, or the presence of a barrier. Temperature-dependent admittance measurements would be needed to definitively confirm this.

To summarise this work, several instabilities were observed in high-Ga, high-Ag ACIGS devices using EQE and JV measurements. Room temperature capaci-

tance measurements revealed that the root cause for the large variations in J_{SC} due to storage and accelerated ageing, and the losses in V_{OC} due to LS, was doping modifications. What could not be determined from these measurements was what mechanism(s) lay behind the doping changes. As discussed in section 3, a first step to learn more would be to perform temperature-dependent admittance spectroscopy, to identify steps and observe for variations after treatments. If steps are observed, bias dependence would be the next property to test, in order to attempt identification of the step cause. The measurements performed thus far indicate that defect origins are more likely than barriers, but it is important to confirm this before attempting to extract activation energies from temperature-dependent admittance spectra. In addition to defect-driven mechanisms, another possibility considered was ion migration in the absorber layer, particularly Ag and Na, which are known to be highly mobile. 'Cycling' of LS treatments and repeated CV sweeps indicated that repeated measurement sweeps in the forward direction increased the doping slightly, whilst repeated reverse direction sweeps decreased the doping. Such results indicated that mobile ions could well be playing a role, so longer duration bias tests were performed, exposing the samples to ± 1.0 V pulses for 15 s followed by a CV measurement of a single point with $V_{DC} = 0$ V in an attempt to develop a transient without significantly perturbing the measurement state ($\delta V = 15$ mV and the measurement took < 3 s). Secondary measurements of bias effects without intermediate measurements indicated the same trends, so we can assume that the effect of measurement was negligible on the bias effect. It was observed that both forward and reverse bias exposure induced a significant doping increase for high-Ga, high-Ag samples (fig.15). Though somewhat unexpected, this result indicated that directional ion migration across the bulk of the absorber is not the culprit causing the stability phenomena. A difference between relaxation for forward and reverse bias can be observed, however, with a reduced recovery from forward bias treatment, and a slow (1000 s) relaxation to a state with reduced doping than the initial state. Cooling the device to 150 K (below the dopant ionisation temperature) revealed a much more subdued and slightly directional response to bias stress, further indicating that the bias response relates to carriers and defects, perhaps requiring thermal energy to overcome an activation barrier.

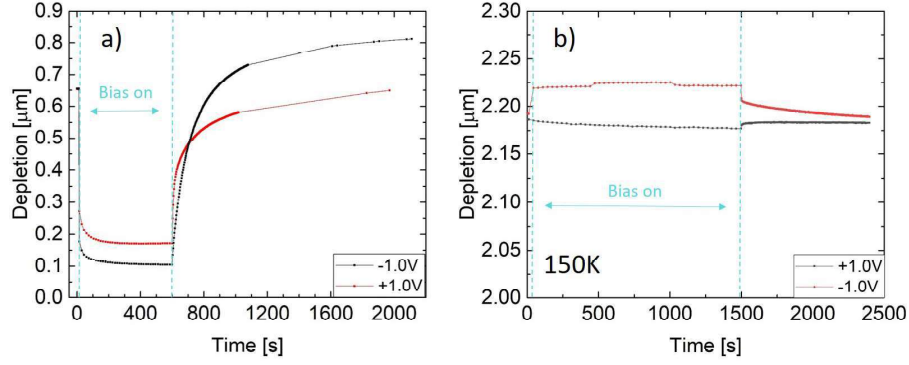


Figure 15: Response of depletion width to forward and reverse bias treatments at room temperature (a) and 150K (b). Dopant ionisation is believed to be incomplete at 150K, as indicated by complete device depletion.

Similar transients were measured under white-LS conditions, revealing a rapid partial recovery of the doping state and a slower relaxation of doping below the initial state. Doping reduction induced by LS was clearly seen in the cycling measurements, where it appeared that white-LS would induce a stable reduction in doping, that was not removed by annealing, leaving the sample for twenty-four hours, or by bias stress (doping increase was observed during bias application, but immediately ceased when bias was removed). The extent to which repeated measurement sweeps could increase/decrease the doping also seemed to be imposed by white-LS treatment. These observations are not yet understood, but indicate a meta-stable phenomenon unobserved in low-Ga, low-Ag (A)CIGS.

4.4 Paper Three - Ag and Ga Impact on ACIGS

In an attempt to clarify the results from the study on the effect of stoichiometry on the stability of high-Ga, high-Ag ACIGS, and determine whether Ag and Ga play dominant roles in the (meta-)stability observed, additional samples were produced. The new samples include high-Ga, high-Ag ACIGS; Ga-free, high-Ag ACIS; high-Ga CIGS and Ga-free, Ag-free CIS. For these samples, $AAC \approx 0.50$, $GGI \approx 0.75$ for 'high' element contents. In order to most clearly compare the sample sets, stoichiometry was chosen to cover the highly responsive region that was observed in the previous work ($0.80 < I/III < 0.92$).

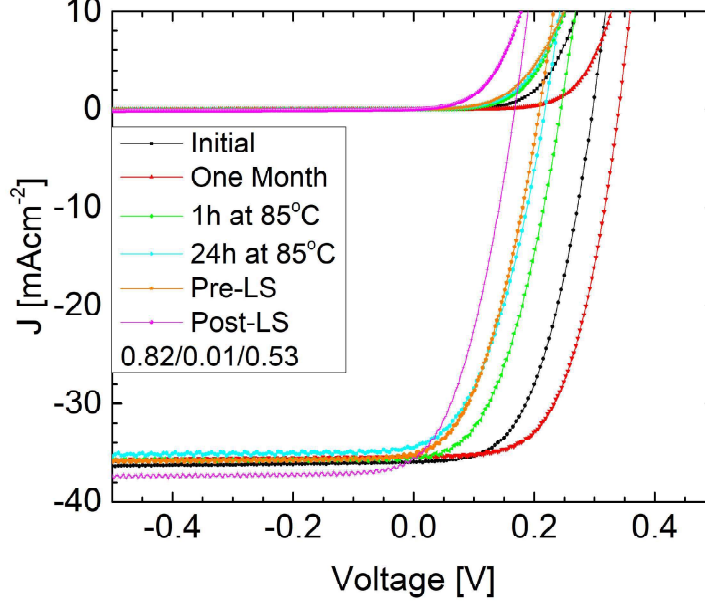


Figure 16: JV measurements of a moderately off-stoichiometric, high-Ag ACIS device over a range of treatments. Note the stability of J_{SC} and strong dependence of V_{OC} on treatment.

Initial results indicate that Ag plays a significant role in (meta-)stability, as a storage period of one month resulted in J_{SC} gains for the ACIGS samples, as opposed to the large losses previously observed. It is also noted that losses such as were observed in the first study are not reported in literature, where typically $AAC \leq 0.25$. Thus, we can suggest that there is a threshold at $AAC \approx 0.50$ where stability behaviour may begin to change. Furthermore, Ga-free ACIS samples show improvements in V_{OC} and FF with time, followed by decreases in these properties after annealing at 85°C and white-LS (fig.16). For high-Ga, high-Ag ACIGS, it is rather seen that J_{SC} is the primarily effected output parameter for annealing and storage. For both materials, however, it seems clear that N_{CV} is the key property leading to output parameter variation. Neither the CIS nor the high-Ga CIGS exhibited notable losses or gains as a response to storage, annealing or white-LS. Consequently, it can be concluded that Ga content also plays a role in stability, in the presence of large fractions of Ag. As with the previous study, more in depth capacitance measurements are required to attempt to unravel the causes of the observed phenomena.

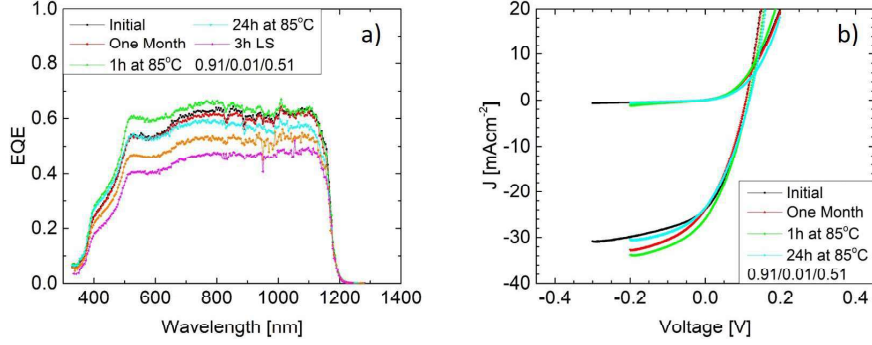


Figure 17: EQE (a) and JV (b) measurements on a close- or over-stoichiometric, high-Ag ACIS device over a range of treatments. Note the extreme voltage dependent collection in the JV profiles and flat EQE spectra, indicating charge transport barriers at the interface.

An additional observation that has been made so far in this study is that over-stoichiometric, high-Ag ACIS devices appear to be limited by interface recombination. Such a deduction can be made from the very 'flat' EQE spectra measured for these devices, in combination with the poor JV performance, very low FF of 30 – 35 % and extreme voltage-dependent collection (fig.17). To further investigate this inference, JVT measurements could be performed to evaluate the dominant recombination activation energy, as detailed in section 2.1. A performance-limiting interface for over-stoichiometric material is also seen in Ag-free CIGS, as briefly described in section 1.2.

5 Summary and Outlook

To conclude, key electrical characterisation techniques have been described, with an exploration of some of the deeper understandings that can be yielded from these measurements, in addition to a mention of potential limitations. Supplementing the theoretical description of the characterisation techniques is a series of examples from my work which illustrate how the measurements can be used in concert in an attempt to understand and evaluate complex phenomena. A proposed workflow for the effective characterisation and understanding of thin-film solar cells follows, informed and motivated by my work with (A)CIGS, but applicable to other materials too:

EQE and JV measurements should form the basis of any investigation into device behaviour and characteristics. Apart from providing useful trackers for behaviour change, and indicators of where to look for the origins of changes, in the form of the output parameters, these measurements provide a wealth of

qualitative information through simple inspection. One can also extract more detailed parameters from the data, giving a quantitative set of values to the visually inspected inferences, for example $\eta_C(V)$, n , and the resistances R_{SH} , R_S . Depending on the observations made, the application of additional voltage- or light-bias during measurement can be a logical next step, and may provide information on meta-stabilities and also their likely location in the device.

If meta-stabilities are observed, or there is an intention to apply treatments to samples and track changes, or compare responses between samples, then it is wise to perform capacitance measurements to evaluate doping and defect responses. In addition to the measurement parameters discussed in section 3.1, it is important to consider the presence of hysteresis in the samples. In the case of high-Ga, high-Ag ACIGS, there is a significant hysteresis effect observed in CV measurements, meaning that in order to evaluate the impact of treatments on doping and depletion, it is wise to measure first a zero-bias ($V_{DC} = 0$) measurement point, such that the application of bias during a sweep does not introduce a measurement perturbation into the system. Such a procedure is also wise in the case of a device exhibiting meta-stable voltage-stress responses. The process I have now adopted is to measure a zero-bias CV point, perform an admittance measurement, repeat the zero-bias CV point, if admittance reveals that the original f_{CV} was inappropriate (default value of 60 kHz). After this initial, hopefully perturbation free, characterisation, CV sweeps in both forward and reverse direction are performed, with a final zero-bias CV point to evaluate sweep-induced variation. In the case of non-negligible hysteresis or voltage-response, it is advised that for subsequent measurement stages, the first measurement should be EQE, due to its minimal perturbation of the system. In my work, the capacitance procedure outlined above follows the EQE measurement, as doping is the primary tracked parameter and has been observed to vary after voltage or illumination exposure, so a JV measurement would perturb the system and change the post-treatment state. The same is, of course, true for CV sweeps, but these are performed on only a few select cells on each sample, whereas the JV illumination will affect every cell on the sample, unless masking is applied, though this adds unnecessary complication.

Already by following this procedure and remaining at room temperature, a large amount of insight can be gained into device behaviour and possible internal mechanisms that lead to the macro-scale effects observed. By combining measurement inferences and literature reports (unfortunately there is a lack of work into high-Ag ACIS and ACIGS), particularly theoretical works, one can focus on several possible theories and begin to explore how further experiments can be designed to rule-out or isolate individual explanations. Of course a powerful tool for these exploratory measurements are the more advanced voltage- and temperature-dependent capacitance techniques, which provide information on potentially significant defects or barriers in the devices. Beyond this, optical techniques such as photoluminescence can also yield valuable and complementary data.

For my work on the stability of ACIGS, it has thus far been discovered, or at the very least is suspected, that high Ag content ($AAC > 0.50$) leads to significant stability issues, however instability and meta-stability are still observed for $AAC \approx 0.50$ which need to be understood. Moreover, the presence of large Ga fractions $GGI > 0.70$ seems to influence the (meta-)stability situation, compared to Ga-free ACIS samples, switching the focus from J_{SC} degradation to V_{OC} and FF fluctuations. A logical next step is to produce a sample set of ACIS and ACIGS devices, with a range of Ga and Ag fractions. The primary goals would be to identify a threshold for AAC stability and to establish a similar threshold for GGI . If, in the course of such an investigation, a trend and clear difference was confirmed, the more advanced capacitance techniques would be implemented to try and evaluate if a change to the defect landscape is enacted through Ag and Ga variation, and if this could perhaps be the root of the issues we observe. An additional experiment which should provide a relatively simple and quick way to exclude one possible contributor to stability issues, is to produce high-Ag, high-Ga ACIGS devices on SLG, Na-free glass, and perhaps including heavy alkalis without Na. The high mobility of Na and its tendency to segregate preferentially to OVCs (which are present in high quantity in our off-stoichiometric material) mean that it could still play a role, despite our initial measurements indicating that bulk migration is unlikely. In- or out-diffusion from grain boundaries or OVCs is a possibility that should not be ruled out.

References

- [1] “Summary for policymakers,” in *Climate Change 2021: The Physical Science Basis. Contribution of Working Group I to the Sixth Assessment Report of the Intergovernmental Panel on Climate Change* (V. Masson-Delmotte, P. Zhai, A. Pirani, S. Connors, C. Péan, S. Berger, N. Caud, Y. Chen, L. Goldfarb, M. Gomis, M. Huang, K. Leitzell, E. Lonnoy, J. Matthews, T. Maycock, T. Waterfield, O. Yelekçi, R. Yu, and B. Zhou, eds.), pp. 3–32, Cambridge, United Kingdom and New York, NY, USA: Cambridge University Press, 2021.
- [2] E. Kabir, P. Kumar, S. Kumar, A. A. Adelodun, and K.-H. Kim, “Solar energy: Potential and future prospects,” *Renewable and Sustainable Energy Reviews*, vol. 82, pp. 894–900, 2018.
- [3] C. Kost, S. Shammugam, V. Fluri, D. Peper, A. D. Memar, and T. Schleg, “Study: Levelized Cost of Electricity - Renewable Energy Technologies - Fraunhofer ISE.”
- [4] “Photovoltaics Report - Fraunhofer ISE.”
- [5] K. Mertens, *Photovoltaics : fundamentals, technology and practice*. Chichester, West Sussex, UK: Wiley, second edition. ed., 2019.

- [6] H. M. Wikoff, S. B. Reese, and M. O. Reese, “Embodied energy and carbon from the manufacture of cadmium telluride and silicon photovoltaics,” *Joule*, vol. 6, no. 7, pp. 1710–1725, 2022.
- [7] P. Jackson, R. Wuerz, D. Hariskos, E. Lotter, W. Witte, and M. Powalla, “Effects of heavy alkali elements in Cu(In,Ga)Se₂ solar cells with efficiencies up to 22.6%,” *Phys. Status Solidi RRL*, vol. 10, no. 8, pp. 583–586, 2016.
- [8] M. A. Green, E. D. Dunlop, J. Hohl-Ebinger, M. Yoshita, N. Kopidakis, K. Bothe, D. Hinken, M. Rauer, and X. Hao, “Solar cell efficiency tables (Version 60),” *Progress in Photovoltaics: Research and Applications*, vol. 30, no. 7, pp. 687–701, 2022.
- [9] W. Shockley and H. J. Queisser, “Detailed balance limit of efficiency of p-n junction solar cells,” *J. Appl. Phys.*, vol. 32, no. 3, pp. 510–519, 1961.
- [10] T. Leijtens, K. A. Bush, R. Prasanna, and M. D. McGehee, “Opportunities and challenges for tandem solar cells using metal halide perovskite semiconductors,” *Nat. Energy*, vol. 3, no. 10, pp. 828–838, 2018.
- [11] J. L. Shay, S. Wagner, and H. M. Kasper, “Efficient CuInSe₂/CdS solar cells,” *Applied Physics Letters*, vol. 27, no. 2, pp. 89–90, 1975.
- [12] R. Scheer and H.-W. Schock, *Introduction*, ch. 1, pp. 1–8. John Wiley & Sons, Ltd, 2011.
- [13] A. M. Gabor, J. R. Tuttle, D. S. Albin, M. A. Contreras, R. Noufi, and A. M. Hermann, “High-efficiency CuIn_xGa_{1-x}Se₂ solar cells made from (In_xGa_{1-x})₂Se₃ precursor films,” *Applied Physics Letters*, vol. 65, no. 2, pp. 198–200, 1994.
- [14] C. Chang, A. Davydov, B. Stanbery, and T. Anderson, “Thermodynamic assessment of the Cu-In-Se system and application to thin film photovoltaics,” in *Conference Record of the Twenty Fifth IEEE Photovoltaic Specialists Conference - 1996*, pp. 849–852, 1996.
- [15] T.-P. Hsieh, C.-C. Chuang, C.-S. Wu, J.-C. Chang, J.-W. Guo, and W.-C. Chen, “Effects of residual copper selenide on CuInGaSe₂ solar cells,” *Solid-State Electronics*, vol. 56, no. 1, pp. 175–178, 2011.
- [16] H. Wilhelm, H.-W. Schock, and R. Scheer, “Interface recombination in heterojunction solar cells: Influence of buffer layer thickness,” *Journal of Applied Physics*, vol. 109, no. 8, p. 084514, 2011.
- [17] M. Turcu, O. Pakma, and U. Rau, “Interdependence of absorber composition and recombination mechanism in Cu(In,Ga)(Se,S)₂ heterojunction solar cells,” *Applied Physics Letters*, vol. 80, no. 14, pp. 2598–2600, 2002.

- [18] S. Siebentritt, L. Gütay, D. Regesch, Y. Aida, and V. Deprédurand, “Why do we make Cu(In,Ga)Se₂ solar cells non-stoichiometric?,” *Solar Energy Materials and Solar Cells*, vol. 119, pp. 18–25, 2013. Thin-film Photovoltaic Solar Cells.
- [19] S.-H. Wei, S. B. Zhang, and A. Zunger, “Effects of Na on the electrical and structural properties of CuInSe₂,” *Journal of Applied Physics*, vol. 85, no. 10, pp. 7214–7218, 1999.
- [20] W. Li, X. Yan, A. G. Aberle, and S. Venkataraj, “Effect of sodium diffusion on the properties of CIGS solar absorbers prepared using elemental Se in a two-step process,” *Scientific Reports*, vol. 9, p. 2637, Dec. 2019.
- [21] D. Rudmann, A. F. da Cunha, M. Kaelin, F. Kurdesau, H. Zogg, A. N. Tiwari, and G. Bilger, “Efficiency enhancement of Cu(In,Ga)Se₂ solar cells due to post-deposition Na incorporation,” *Applied Physics Letters*, vol. 84, no. 7, pp. 1129–1131, 2004.
- [22] A. Chirilă, P. Reinhard, F. Pianezzi, P. Bloesch, A. R. Uhl, C. Fella, L. Kranz, D. Keller, C. Gretener, H. Hagendorfer, D. Jaeger, R. Erni, S. Nishiwaki, S. Buecheler, and A. N. Tiwari, “Potassium-induced surface modification of Cu(In,Ga)Se₂ thin films for high-efficiency solar cells,” *Nature Materials* 2013 12:12, vol. 12, pp. 1107–1111, 11 2013.
- [23] Y. Sun, S. Lin, W. Li, S. Cheng, Y. Zhang, Y. Liu, and W. Liu, “Review on alkali element doping in Cu(In,Ga)Se₂ thin films and solar cells,” *Engineering*, vol. 3, no. 4, pp. 452–459, 2017.
- [24] S. Wei and A. Zunger, “Band offsets and optical bowings of chalcopyrites and Zn-based II-VI alloys,” *Journal of Applied Physics*, vol. 78, no. 6, pp. 3846–3856, 1995.
- [25] R. Herberhotz, H. Schock, U. Rau, J. Werner, T. Haalboom, T. Godecke, F. Ernst, C. Beilharz, K. Benz, and D. Cahen, “New aspects of phase segregation and junction formation in CuInSe₂,” in *Conference Record of the Twenty Sixth IEEE Photovoltaic Specialists Conference - 1997*, pp. 323–326, 1997.
- [26] S. Schleussner, U. Zimmermann, T. Wätjen, K. Leifer, and M. Edoff, “Effect of gallium grading in Cu(In,Ga)Se₂ solar-cell absorbers produced by multi-stage coevaporation,” *Solar Energy Materials and Solar Cells*, vol. 95, no. 2, pp. 721–726, 2011.
- [27] A. Dhingra and A. Rothwarf, “Computer simulation and modeling of the graded bandgap CuInSe₂CdS solar cell,” in *Conference Record of the Twenty Third IEEE Photovoltaic Specialists Conference - 1993 (Cat. No.93CH3283-9)*, pp. 475–480, 1993.

- [28] T. Kobayashi, H. Yamaguchi, Z. Jehl Li Kao, H. Sugimoto, T. Kato, H. Hakuma, and T. Nakada, “Impacts of surface sulfurization on $\text{Cu}(\text{In}_{1-x}\text{Ga}_x)\text{Se}_2$ thin-film solar cells,” *Progress in Photovoltaics: Research and Applications*, vol. 23, no. 10, pp. 1367–1374, 2015.
- [29] P. T. Erslev, J. Lee, G. M. Hanket, W. N. Shafarman, and J. D. Cohen, “The electronic structure of $\text{Cu}(\text{In}_{1-x}\text{Ga}_x)\text{Se}_2$ alloyed with silver,” *Thin Solid Films*, vol. 519, pp. 7296–7299, 8 2011.
- [30] M. A. Contreras, L. M. Mansfield, B. Egaas, J. Li, M. Romero, R. Noufi, E. Rudiger-Voigt, and W. Mannstadt, “Wide bandgap $\text{Cu}(\text{In,Ga})\text{Se}_2$ solar cells with improved energy conversion efficiency,” *Prog. Photovoltaics*, vol. 20, no. 7, pp. 843–850, 2012.
- [31] G. Hanna, A. Jasenek, U. Rau, and H. Schock, “Influence of the Ga-content on the bulk defect densities of $\text{Cu}(\text{In,Ga})\text{Se}_2$,” *Thin Solid Films*, vol. 387, no. 1, pp. 71–73, 2001.
- [32] C. Spindler, F. Babbe, M. H. Wolter, F. Ehré, K. Santhosh, P. Hilgert, F. Werner, and S. Siebentritt, “Electronic defects in $\text{Cu}(\text{In,Ga})\text{Se}_2$: towards a comprehensive model,” *Phys. Rev. Materials*, vol. 3, p. 090302, Sep 2019.
- [33] J. V. Li, S. Grover, M. A. Contreras, K. Ramanathan, D. Kuciauskas, and R. Noufi, “A recombination analysis of $\text{Cu}(\text{In,Ga})\text{Se}_2$ solar cells with low and high Ga compositions,” *Sol. Energy Mater. Sol. Cells*, vol. 124, pp. 143–149, 5 2014.
- [34] T. Minemoto, T. Matsui, H. Takakura, Y. Hamakawa, T. Negami, Y. Hashimoto, T. Uenoyama, and M. Kitagawa, “Theoretical analysis of the effect of conduction band offset of window/CIS layers on performance of CIS solar cells using device simulation,” *Sol. Energy Mater. Sol. Cells*, vol. 67, no. 1, pp. 83–88, 2001. PVSEC 11 - PART III.
- [35] M. Raghuwanshi, E. Cadel, P. Pareige, S. Duguay, F. Couzinie-Devy, L. Arzel, and N. Barreau, “Influence of grain boundary modification on limited performance of wide bandgap $\text{Cu}(\text{In,Ga})\text{Se}_2$ solar cells,” *Appl. Phys. Lett.*, vol. 105, no. 1, p. 013902, 2014.
- [36] M. Raghuwanshi, R. Wuerz, and O. Cojocaru-Mirédin, “Interconnection between trait, structure, and composition of grain boundaries in $\text{Cu}(\text{In,Ga})\text{Se}_2$ thin-film solar cells,” *Adv. Funct. Mater.*, vol. 30, 8 2020.
- [37] M. Balboul, H. Schock, S. Fayak, A. A. El-Aal, J. Werner, and A. Ramadan, “Correlation of structure parameters of absorber layer with efficiency of $\text{Cu}(\text{In,Ga})\text{Se}_2$ solar cell,” *Appl. Phys. A*, vol. 92, no. 3, pp. 557–563, 2008.
- [38] J. Keller, K. V. Sopiha, O. Stolt, L. Stolt, C. Persson, J. J. Scragg, T. Törndahl, and M. Edoff, “Wide-gap $(\text{Ag,Cu})(\text{In,Ga})\text{Se}_2$ solar cells with

- different buffer materials— A path to a better heterojunction,” *Prog. Photovoltaics*, vol. 28, pp. 237–250, 4 2020.
- [39] W. Shafarman, C. Thompson, J. Boyle, G. Hanket, P. Erslev, and J. David Cohen, “Device characterization of (Ag,Cu)(In,Ga)Se₂ solar cells,” in *2010 35th IEEE Photovoltaic Specialists Conference*, pp. 000325–000329, 2010.
 - [40] T. Nishimura, A. Doi, J. Chantana, A. Mavlonov, Y. Kawano, and T. Minemoto, “Silver-alloyed wide-gap CuGaSe₂ solar cells,” *Sol. Energy*, vol. 230, pp. 509–514, 12 2021.
 - [41] C. Wang, D. Zhuang, M. Zhao, Y. Li, L. Dong, H. Wang, J. Wei, and Q. Gong, “Effects of silver-doping on properties of Cu(In,Ga)Se₂ films prepared by CuInGa precursors,” *J. Energy Chem.*, vol. 66, pp. 218–225, 3 2022.
 - [42] G. Kim, W. M. Kim, J. K. Park, D. Kim, H. Yu, and J. H. Jeong, “Thin ag precursor layer-assisted co-evaporation process for low temperature growth of Cu(In,Ga)Se₂ thin film,” *ACS Applied Materials and Interfaces*, vol. 11, pp. 31923–31933, 9 2019.
 - [43] S. C. Yang, T. Y. Lin, M. Ochoa, H. Lai, R. Kothandaraman, F. Fu, A. N. Tiwari, and R. Carron, “Efficiency boost of bifacial Cu(In,Ga)Se₂ thin-film solar cells for flexible and tandem applications with silver-assisted low-temperature process,” *Nature Energy*, 2022.
 - [44] J. Keller, H. Aboulfadl, L. Stolt, O. Donzel-Gargand, and M. Edoff, “Rubidium fluoride absorber treatment for wide-gap (Ag,Cu)(In,Ga)Se₂ solar cells,” *Solar RRL*, vol. 6, no. 6, p. 2200044, 2022.
 - [45] R. Wang, B. Dou, Y. Zheng, and S.-H. Wei, “Investigation of Ag(Ga,In)Se₂ as thin-film solar cell absorbers: A first-principles study,” *Science China Physics, Mechanics & Astronomy*, vol. 65, p. 107311, Aug. 2022.
 - [46] M. Edoff, T. Jarmar, N. S. Nilsson, E. Wallin, D. Högström, O. Stolt, O. Lundberg, W. Shafarman, and L. Stolt, “High Voc in (Cu,Ag)(In,Ga)Se₂ Solar Cells,” *IEEE Journal of Photovoltaics*, vol. 7, pp. 1789–1794, Nov. 2017.
 - [47] V. Fjällström, P. M. Salome, A. Hultqvist, M. Edoff, T. Jarmar, B. G. Aitken, K. Zhang, K. Fuller, and C. K. Williams, “Potential-induced degradation of CuIn_{1-x}Ga_xSe₂ thin film solar cells,” *IEEE Journal of Photovoltaics*, vol. 3, pp. 1090–1094, 2013.
 - [48] J. F. Guillemoles, L. Kronik, D. Cahen, U. Rau, A. Jasenek, and H. W. Schock, “Stability issues of Cu(In,Ga)Se₂-based solar cells,” *Journal of Physical Chemistry B*, vol. 104, pp. 4849–4862, 5 2000.

- [49] M. Theelen, V. Hans, N. Barreau, H. Steijvers, Z. Vroon, and M. Zeman, “The impact of alkali elements on the degradation of CIGS solar cells,” *Progress in Photovoltaics: Research and Applications*, vol. 23, no. 5, pp. 537–545, 2015.
- [50] J. Nishinaga, T. Koida, S. Ishizuka, Y. Kamikawa, H. Takahashi, M. Iioka, H. Higuchi, Y. Ueno, H. Shibata, and S. Niki, “Effects of long-term heat-light soaking on Cu(In,Ga)Se₂ solar cells with kf postdeposition treatment,” *Applied Physics Express*, vol. 10, p. 092301, aug 2017.
- [51] P. Pearson, J. Keller, J. Larsen, V. Kosyak, and C. Platzer-Björkman, “Long term stability and recovery of 3 MeV proton irradiated Cu(In,Ga)Se₂ and Cu₂(Zn,Sn)(S,Se)₄ thin film solar cells,” *Thin Solid Films*, vol. 741, p. 139023, 2022.
- [52] U. Rau, M. Schmitt, J. Parisi, W. Riedl, and F. Karg, “Persistent photoconductivity in Cu(In,Ga)Se₂ heterojunctions and thin films prepared by sequential deposition,” *Applied Physics Letters*, vol. 73, no. 2, pp. 223–225, 1998.
- [53] M. Igalson, A. Urbaniak, P. Zabierowski, H. A. Maksoud, M. Buffiere, N. Barreau, and S. Spiering, “Red-blue effect in Cu(In,Ga)Se₂-based devices revisited,” vol. 535, pp. 302–306, 5 2013.
- [54] H. Tangara, Y. He, M. M. Islam, S. Ishizuka, and T. Sakurai, “Analysis of the combined effect of long-term heat light soaking and KF/NaF post-deposition treatment on the open-circuit voltage loss in CIGS solar cells,” *Japanese Journal of Applied Physics*, vol. 61, p. SC1050, feb 2022.
- [55] S. Lany and A. Zunger, “Light- and bias-induced metastabilities in Cu(In,Ga)Se₂ based solar cells caused by the (V_{Se}-V_{Cu}) vacancy complex,” *J. Appl. Phys.*, vol. 100, 2006.
- [56] M. Igalson, M. Maciaszek, K. Macielak, A. Czudek, M. Edoff, and N. Barreau, “Concentration of defects responsible for persistent photoconductivity in Cu(In,Ga)Se₂: Dependence on material composition,” *Thin Solid Films*, vol. 669, pp. 600–604, 1 2019.
- [57] A. Urbaniak and M. Igalson, “Creation and relaxation of light- and bias-induced metastabilities in Cu(In,Ga)Se₂,” *Journal of Applied Physics*, vol. 106, no. 6, p. 063720, 2009.
- [58] J. Pohl and K. Albe, “Intrinsic point defects in CuInSe₂ and CuGaSe₂ as seen via screened-exchange hybrid density functional theory,” *Physical Review B - Condensed Matter and Materials Physics*, vol. 87, 6 2013.
- [59] J. Coutinho, V. P. Markevich, and A. R. Peaker, “Characterisation of negative-U defects in semiconductors,” *Journal of Physics: Condensed Matter*, vol. 32, p. 323001, may 2020.

- [60] M. Igalson, P. Zabierowski, D. Przado, A. Urbaniak, M. Edoff, and W. N. Shafarman, “Understanding defect-related issues limiting efficiency of CIGS solar cells,” *Solar Energy Materials and Solar Cells*, vol. 93, no. 8, pp. 1290–1295, 2009.
- [61] S. Lany and A. Zunger, “Limitation of the open-circuit voltage due to metastable intrinsic defects in Cu(In,Ga)Se₂ and strategies to avoid these defects,” in *2008 33rd IEEE Photovoltaic Specialists Conference*, pp. 1–3, 2008.
- [62] A. Czudek, A. Urbaniak, A. Eslam, R. Wuerz, and M. Igalson, “Dependence of the magnitude of persistent photoconductivity on sodium content in Cu(In,Ga)Se₂ solar cells and thin films,” *IEEE Journal of Photovoltaics*, vol. 10, pp. 1926–1930, 11 2020.
- [63] M. Cwil, M. Igalson, P. Zabierowski, and S. Siebentritt, “Charge and doping distributions by capacitance profiling in Cu(In,Ga)Se₂ solar cells,” *Journal of Applied Physics*, vol. 103, no. 6, p. 063701, 2008.
- [64] A. J. Ferguson, R. Farshchi, P. K. Paul, P. Dippo, J. Bailey, D. Poplavskyy, A. Khanam, F. Tuomisto, A. R. Archart, and D. Kuciauskas, “Defect-mediated metastability and carrier lifetimes in polycrystalline (Ag,Cu)(In,Ga)Se₂ absorber materials,” *J. Appl. Phys.*, vol. 127, 6 2020.
- [65] A. Ferguson, P. Dippo, D. Kuciauskas, R. Farshchi, J. Bailey, G. Zapalac, and D. Poplavskyy, “Optical spectroscopic probes of degradation and metastability in polycrystalline (Ag,Cu)(In,Ga)Se₂ absorbers,” in *2018 IEEE 7th World Conference on Photovoltaic Energy Conversion (WCPEC)*, pp. 3918–3922, 2018.
- [66] S. Lany and A. Zunger, “Intrinsic dx centers in ternary chalcopyrite semiconductors,” *Phys. Rev. Lett.*, vol. 100, 1 2008.
- [67] M. Igalson, M. Bodegård, and L. Stolt, “Reversible changes of the fill factor in the ZnO/CdS/Cu(In,Ga)Se₂ solar cells,” *Solar Energy Materials and Solar Cells*, vol. 80, no. 2, pp. 195–207, 2003.
- [68] P. Pearson, J. Keller, L. Stolt, M. Edoff, and C. Platzer Björkman, “The effect of absorber stoichiometry on the stability of widegap (Ag,Cu)(In,Ga)Se₂ solar cells,” *physica status solidi (b)*, vol. 259, no. 11, p. 2200104, 2022.
- [69] S. S. Hegedus and W. N. Shafarman, “Thin-film solar cells: Device measurements and analysis,” *Progress in Photovoltaics: Research and Applications*, vol. 12, pp. 155–176, 2004.
- [70] S. Hegedus, D. Desai, and C. Thompson, “Voltage dependent photocurrent collection in CdTe/CdS solar cells,” *Progress in Photovoltaics: Research and Applications*, vol. 15, pp. 587–602, 11 2007.

- [71] F. Werner, F. Babbe, H. Elanzeery, and S. Siebentritt, “Can we see defects in capacitance measurements of thin-film solar cells?,” *Progress in Photovoltaics: Research and Applications*, vol. 27, pp. 1045–1058, 11 2019.
- [72] J. Heath and P. Zabierowski, *Capacitance Spectroscopy of Thin-Film Solar Cells*, ch. 4, pp. 81–105. John Wiley & Sons, Ltd, 2011.
- [73] J. T. Heath, “Capacitance-voltage and drive-level-capacitance profiling,” in *Capacitance Spectroscopy of Semiconductors*, pp. 85–113, Jenny Stanford Publishing, 2018.
- [74] W. Johnson and P. Panousis, “The influence of debye length on the C-V measurement of doping profiles,” *IEEE Transactions on Electron Devices*, vol. 18, no. 10, pp. 965–973, 1971.
- [75] J. H. Scofield, “Effects of series resistance and inductance on solar cell admittance measurements,” *J.H. Scof@ld /Solar Energy Material and Solar Cells*, vol. 37, pp. 217–233, 1995.
- [76] J. Heath and P. Zabierowski, “Capacitance spectroscopy of thin-film solar cells,” *Advanced characterization techniques for thin film solar cells*, vol. 1, pp. 93–119, 2016.
- [77] P. Paul, J. Bailey, G. Zapalac, and A. Arehart, “Fast C-V method to mitigate effects of deep levels in CIGS doping profiles,” in *2017 IEEE 44th Photovoltaic Specialist Conference (PVSC)*, pp. 2414–2418, 2017.
- [78] M. Ćwil, M. Igalson, P. Zabierowski, C. A. Kaufmann, and A. Neisser, “Capacitance profiling in the CIGS solar cells,” *Thin Solid Films*, vol. 515, pp. 6229–6232, 5 2007.
- [79] T. P. Weiss, S. Nishiwaki, B. Bissig, S. Buecheler, and A. N. Tiwari, “Voltage dependent admittance spectroscopy for the detection of near interface defect states for thin film solar cells,” *Physical Chemistry Chemical Physics*, vol. 19, no. 45, pp. 30410–30417, 2017.
- [80] S. Ravishankar, T. Unold, and T. Kirchartz, “Comment on resolving spatial and energetic distributions of trap states in metal halide perovskite solar cells,” *Science*, vol. 371, no. 6532, p. eabd8014, 2021.
- [81] F. Werner, M. H. Wolter, S. Siebentritt, G. Sozzi, S. Di Napoli, R. Menozzi, P. Jackson, W. Witte, R. Carron, E. Avancini, T. P. Weiss, and S. Buecheler, “Alkali treatments of Cu(In,Ga)Se₂ thin-film absorbers and their impact on transport barriers,” *Progress in Photovoltaics: Research and Applications*, vol. 26, no. 11, pp. 911–923, 2018.
- [82] Van Puyvelde, Lisanne, *Electric and optical defect characterisation of Cu₂ZnSnS₄ and CuIn_{1-x}Ga_xSe₂ based thin-film solar cells*. PhD thesis, Ghent University, 2015.

- [83] Y. Y. Proskuryakov, K. Durose, M. K. A. Turkestani, I. Mora-Seró, G. Garcia-Belmonte, F. Fabregat-Santiago, J. Bisquert, V. Barrioz, D. Lamb, S. J. Irvine, and E. W. Jones, “Impedance spectroscopy of thin-film CdTe/CdS solar cells under varied illumination,” *Journal of Applied Physics*, vol. 106, 2009.
- [84] H. Sakakura, M. Itagaki, and M. Sugiyama, “Estimation of defect activation energy around pn interfaces of Cu(In,Ga)Se₂ solar cells using impedance spectroscopy,” *Japanese Journal of Applied Physics*, vol. 55, p. 012301, 1 2016.
- [85] Y. Y. Proskuryakov, K. Durose, B. M. Taelle, G. P. Welch, and S. Oelting, “Admittance spectroscopy of CdTeCdS solar cells subjected to varied nitric-phosphoric etching conditions,” *Journal of Applied Physics*, vol. 101, 2007.
- [86] R. Burgess, W. Chen, W. Devaney, D. Doyle, N. Kim, and B. Stanbery, “Electron and proton radiation effects on GaAs and CuInSe₂ thin film solar cells,” in *Conference Record of the Twentieth IEEE Photovoltaic Specialists Conference*, pp. 909–912, IEEE, 1996.
- [87] S. S. Suvanam, J. Larsen, N. Ross, V. Kosyak, A. Hallén, and C. P. Björkman, “Extreme radiation hard thin film CZTSSe solar cell,” *Solar Energy Materials and Solar Cells*, vol. 185, pp. 16–20, 2018.
- [88] J. Keller, L. Stolt, K. V. Sopiha, J. K. Larsen, L. Riekehr, and M. Edoff, “On the paramount role of absorber stoichiometry in (Ag,Cu)(In,Ga)Se₂ wide-gap solar cells,” *Solar RRL*, vol. 4, no. 12, p. 2000508, 2020.

6 List of Papers

This thesis draws on the data and knowledge gained in the process of producing the following papers. Text and images were reused with permission from the respective publishers.

Paper One:

- "Long term stability and recovery of 3 MeV proton irradiated $\text{Cu}(\text{In,Ga})\text{Se}_2$ and $\text{Cu}_2(\text{Zn,Sn})(\text{S,Se})_4$ thin film solar cells" P. Pearson, J. Keller, J. Larsen, V. Kosyak, C. Platzer-Björkman. *Thin Solid Films* 741 (2022) 139023.

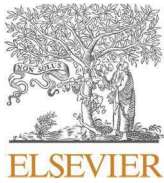
My contributions to this paper were to be the main author and perform the experimental work carried out in 2021 (previous data were collected in 2017).

Paper Two:

- "The Effect of Absorber Stoichiometry on the Stability of Widegap $(\text{Ag,Cu})(\text{In,Ga})\text{Se}_2$ Solar Cells". P. Pearson, J. Keller, L. Stolt, M. Edoff, C. Platzer Björkman. *Phys. Status Solidi B*, 259 : 2200104 (2022).

My contributions to this paper were to be the main author, contribute to the planning and sequence of experiments, and to perform the majority of the experimental work.

Please find the papers attached in the following pages.



Long term stability and recovery of 3 MeV proton irradiated Cu(In,Ga)Se₂ and Cu₂(Zn,Sn)(S,Se)₄ thin film solar cells

Patrick Pearson^{a,*}, Jan Keller^a, Jes Larsen^a, Volodymyr Kosyak^b, Charlotte Platzter-Björkman^a

^a Division of Solar Cell Technology, Department of Materials Science and Engineering, Uppsala University, Box 35, Ångströmlaboratoriet, Lägerhyddsvägen 1 75121, Uppsala 751 03, Sweden

^b Midsummer AB, Elektronikhöjden 6, Järfälla 175 43, Sweden

ARTICLE INFO

Keywords:

Copper indium gallium diselenide
Copper zinc tin sulfide
Copper zinc tin sulphide selenide
Proton irradiation
Radiation hardness
Stability

ABSTRACT

In 2017, Cu(In,Ga)Se₂ (CIGS), Cu₂(Zn,Sn)S₄ (CZTS) and Cu₂(Zn,Sn)(S,Se)₄ (CZTSSe) thin film solar cells were irradiated by our group using 3 MeV protons to investigate the materials' radiation hardness and subsequent recovery following dark storage. It was observed that the primary losses were in open-circuit voltage (V_{OC}), with the CZTS and CZTSSe being more resistant than the CIGS, also recovering to $\sim 95\%$ of initial performance, compared to $\sim 70\%$ for CIGS after two months dark storage. In 2021 the cells were investigated by external quantum efficiency and current-voltage measurements once again, to investigate further recovery. The CIGS cells had continued to recover, whilst the CZTSSe devices appear to have fully recovered from radiation induced damage, but now suffer from aging-related degradation and exhibit slight bandgap widening over time. The CZTS cells were observed to recover fully from the radiation induced damage, whilst also showing gains in V_{OC} .

1. Introduction

One of the first serious commercial applications of solar cells was for use in space. Although the solar energy industry has advanced considerably since this time, space applications are still highly relevant and bring additional challenges that terrestrial installations need not face. Due to their low mass and potential for flexibility, thin film solar cells are highly desirable for use in space, though at present extra-terrestrial solar technology is still limited to Si and GaAs, motivating our interest in investigating the effects of radiation on two key thin-film technologies: the established Cu(In,Ga)Se₂ (CIGS) and emerging Cu₂(Zn,Sn)(S,Se)₄ (CZTS(Se)). It is also hoped that by investigating long-term recovery, further light can be shed on the internal mechanisms of the three materials. It is known that CIGS, CZTS and CZTSSe are considerably more radiation hard than Si or GaAs [1]. There are many reports on the effects of radiation on CIGS (key references being [2–4]), but only very few on CZTS and CZTSSe ([5–7]). One of these, a work by Suvanam, et al. [5] is the predecessor to this study. In this initial work CIGS, CZTS and CZTSSe thin film solar cells were irradiated by 3 MeV protons in an attempt to quantify the radiation hardness of CZTS and CZTSSe and compare them to CIGS when irradiated. The samples were additionally kept in dark conditions for two months, such that the materials' self-recovery

processes could be investigated. It was observed that the primary losses were in open-circuit voltage (V_{OC}), with CZTS and CZTSSe being more resilient than CIGS and recovering to $\sim 95\%$ of initial performance, compared to $\sim 70\%$ for CIGS after the dark storage. After the initial study, the cells were placed in dark storage until 2021, when current-voltage (IV) and external quantum efficiency (EQE) measurements were used to investigate any further recovery, as we report on here.

2. Experimental details

The CIGS absorbers were provided by Solibro AB and grown via a three-stage co-evaporation process. The CZTS and CZTSSe samples were grown as described in [5], with 1100 nm thick CZTS absorber layer and 1250 nm thick CZTSSe absorber. All cells were deposited on 300 nm Mo on soda-lime glass substrates. The CZTS and CZTSSe samples were slightly Cu-poor and Sn-rich ($\text{Cu}/(\text{Zn}+\text{Sn}) = 0.94$ and $\text{Zn}/\text{Sn} = 0.97$). The CZTSSe samples had a bandgap of just over 1.2 eV, corresponding to a sulphur to sulphur-selenium ratio of around 0.4. A 70 nm CdS buffer was applied to all samples via chemical bath deposition, followed by sputtering of a window layer consisting of an 80 nm intrinsic ZnO layer and 210 nm ZnO:Al transparent conducting oxide. The devices were

* Corresponding author.

E-mail address: patrick.pearson@angstrom.uu.se (P. Pearson).

<https://doi.org/10.1016/j.tsf.2021.139023>

Received 17 June 2021; Received in revised form 22 November 2021; Accepted 22 November 2021

Available online 26 November 2021

0040-6090/© 2021 The Author(s). Published by Elsevier B.V. This is an open access article under the CC BY license (<http://creativecommons.org/licenses/by/4.0/>).

irradiated by 3 MeV protons at fluences of $\Phi = 10^{10}$, 10^{11} , 10^{12} and 10^{13} cm^{-2} at the Tandem Lab, Uppsala University (a constant proton flux was maintained with samples irradiated for a time sufficient to reach the specified fluence, this was in the order of ten minutes). This energy was chosen to ensure reasonably uniform absorption throughout the device and avoid localised damage, based on the knowledge that ~ 0.4 MeV is sufficient to penetrate to the rear surface [8]. The irradiation procedure followed the AIAA S-111-2005 "Qualification and Quality Requirements for Space Solar Cells" test standards [9]. In order to investigate the radiation induced effects and long-term recovery, the devices were characterised by IV and EQE measurements. Some devices were also characterised using capacitance-voltage (CV) measurements with an Agilent 4284A Precision LCR Meter and Keithley 2401 Source Meter. Sweep frequency was determined via admittance measurements, using the frequency that brought the phase angle closest to 90° (~ 40 kHz for CIGS samples, ~ 95 kHz for CZTSSe samples and 15–20 kHz for CZTS samples). Measurements were performed in January 2021 and related to measurements performed in November 2017 (prior to irradiation) and January 2018 (immediately after irradiation) [5]. The devices were stored in dark conditions at room temperature. When IV measurements were first performed in 2017, all cells were measured on each sample, with one representative cell chosen for each sample. Only the representative cells went on to have EQE measurements. At all later stages, it was the same representative cells that were characterised by EQE and, in 2021, CV measurements. The IV graphs presented in this work are those of the representative cells. Those measurements taken to evaluate the irradiated state of the samples were performed within an hour of irradiation.

3. Results and discussion

3.1. CIGS

A clear increase in current density-voltage (JV) degradation can be observed as proton fluence increases (Fig. 1), with V_{OC} decreasing by ~ 155 mV for maximum irradiation, from 670 mV to 515 mV (Fig. 1c). A clear recovery in V_{OC} can be observed over the three year extended dark recovery period for the maximally irradiated sample, reaching 575 mV (86% of the as grown value, Fig. 1c). The sample irradiated with a fluence of 10^{12} cm^{-2} also exhibited partial recovery, gaining 10 mV (from 610 mV to 620 mV) and reaching 93% of the as grown value (660 mV, Fig. 1b). The 10^{11} cm^{-2} sample was observed to have suffered only very minimal degradation and no significant gains were measured over the recovery period (Fig. 1a). No irradiation damage was observed for the sample receiving a fluence of 10^{10} cm^{-2} . There is no variation in bandgap after irradiation, so it is to be concluded that irradiation either reduces net doping or increases recombination centre concentration. The EQE response of the sample under maximal irradiation (Fig. 2c) indicates a significant increase in recombination immediately after irradiation, leading to speculation of radiation-induced recombination

centres. However, it is also noted that the EQE response of the 10^{11} cm^{-2} fluence sample was unchanged by irradiation, whilst the 10^{12} cm^{-2} fluence sample suffered only minimal losses (Fig. 2a and b), suggesting that recombination centre creation is at a significantly lower level below a fluence of 10^{13} cm^{-2} . Moreover, it is seen that though the EQE response of the maximally irradiated CIGS sample recovers almost completely after extended dark storage, the V_{OC} recovery remains incomplete, indicating that there is potentially an additional mechanism acting. Indeed, a review of the literature suggests that there is a proton fluence threshold separating a lower and higher damage regime: A study by Kawakita also observed a significant increase in degradation above proton fluences of 10^{12} cm^{-2} , observing significant reductions in net doping. A defect level suspected to correspond to the donor-like In_{Cu} antisite defect was also seen to emerge with irradiation [3]. Similarly, a fluence threshold for increased damage via a transition from shallow compensating defect generation to deep trap state generation was reported by Khatri, et al. [10]. Lee, et al. utilised THz spectroscopy to complement photoluminescence (PL) measurements to investigate the effects of H⁺ radiation on CIGS, observing remarkable reductions in minority-carrier bulk lifetime, pointing towards the generation of non-radiative recombination centres. From Hall measurements they also observed a decrease in both carrier concentration and carrier mobility with irradiation. Surface conversion from *p*- to *n*-type CIGS was also seen [11]. PL studies by Yoshida and Hirose also follow this trend [12,13]. We cannot add evidence to speculation, as no PL or CV measurements were taken in the initial study to allow comparison, though CV profiling performed in 2021 shows only small variations between samples, with net-doping in the region of $0.8\text{--}1.1 \times 10^{16}$ cm^{-3} which is not unusually low [14,15]. Considering that the maximally irradiated sample still exhibits clear V_{OC} degradation, it seems unlikely that reduced carrier concentration is the primary mechanism at play here. It seems most likely that the cause for the observed degradation is an increased density of deep recombination centres.

3.2. CZTSSe

CZTSSe was observed to be much more radiation hard than CIGS, showing minimal degradation, even at the highest level of irradiation (Fig. 3c), losing 8% of V_{OC} compared to 22% (lower fluences caused no V_{OC} degradation for CZTSSe (Fig. 3a)). After extended dark storage, V_{OC} recovery has continued minimally since the initial two month recovery period, remaining around 95% for the 10^{12} cm^{-2} and 10^{13} cm^{-2} fluence levels, though the 10^{11} cm^{-2} irradiated sample now measures an improvement of 5% beyond pre-irradiation V_{OC} . Due to the significant and rapid recovery of radiation damage and the consistent and similar fill-factor (FF) degradation observed across all CZTSSe samples, we speculate that a full recovery from radiation damage has in fact been made, however age-related degradation is now evident in the materials. The sample irradiated with a fluence of 10^{10} cm^{-2} showed no changes immediately after irradiation, however FF degradation similar to the

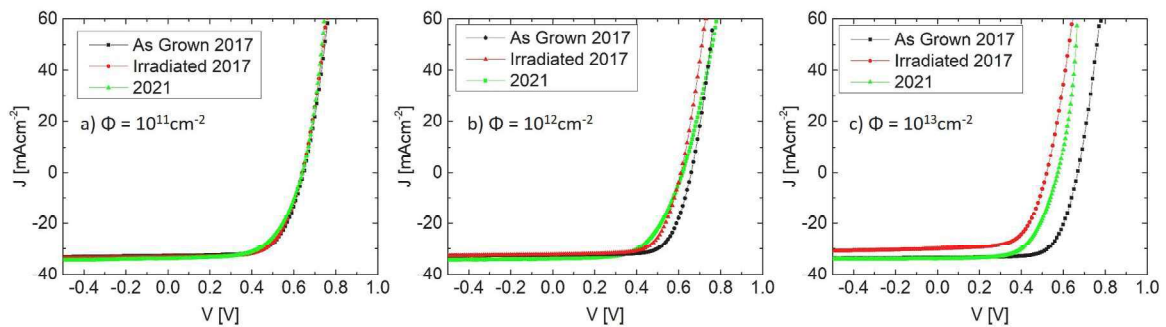


Fig. 1. Light JV curves for each of the CIGS samples, showing clear initial V_{OC} losses, increasing with proton fluence, with subsequent partial recovery. Figure 1c is recreated and extended through addition of new data with the permission of the authors of the initial study [5].

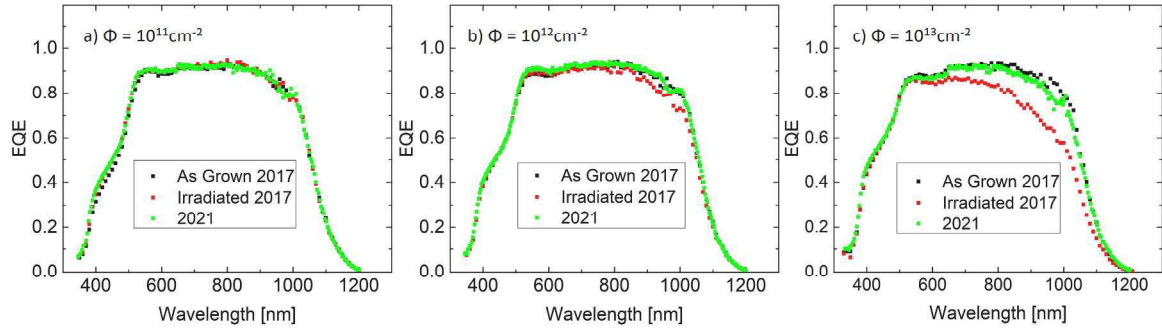


Fig. 2. The EQE response for each of the CIGS samples, showing significant degradation at $\Phi = 10^{13} \text{ cm}^{-2}$, indicating a strong increase in recombination compared to lower fluences. Figure 2c is recreated and extended through addition of new data with the permission of the authors of the initial study [5].

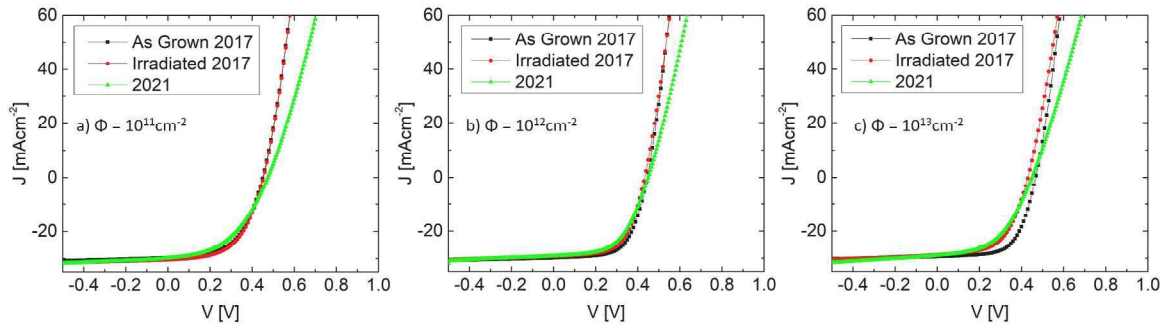


Fig. 3. Light JV curves for each of the CZTSSe samples, showing high levels of radiation hardness and requiring an order of magnitude greater proton fluence to induce damage comparable to the CIGS cells. Near full V_{OC} recovery is observed, but fluence-independent FF degradation is also seen. Figure 3c is recreated and extended through addition of new data with the permission of the authors of the initial study [5].

other samples was observed. A PL study by Sulimov, et al. irradiating CZTSe with high energy electrons (which seem to have similar effects to protons, for CIGS) reported an overall decrease in PL peak intensity and a red-shifting of peak position, consistent with the formation of deep non-radiative recombination centres [7]. This is supported by another work undertaken at Uppsala [16] using similar samples, irradiated with 0.25 MeV protons, and incorporating CV profiling. It was noted that though net doping did decrease upon sample irradiation, the extent to which doping was reduced was insufficient to explain the severe V_{OC} degradation, leading to the conclusion that recombination centres,

rather than doping compensation is responsible for the observed effects. Performing CV profiling on these 0.25 MeV samples now, in 2021, revealed an almost complete recovery of doping levels, CV profiling of the 3 MeV samples reveals small differences in net-doping (of the order $2 \times 10^{15} \text{ cm}^{-3}$). An interesting and unexpected observation from EQE measurements on the CZTSSe samples (Fig. 4) is an apparent increase in bandgap over time for the 10^{12} cm^{-2} fluence sample (Fig. 4a). No changes in EQE were observed immediately after irradiation for this sample (Fig. 4a), but for the 10^{13} cm^{-2} fluence sample, a decrease in the signal for longer wavelengths is observed in addition to a bandgap

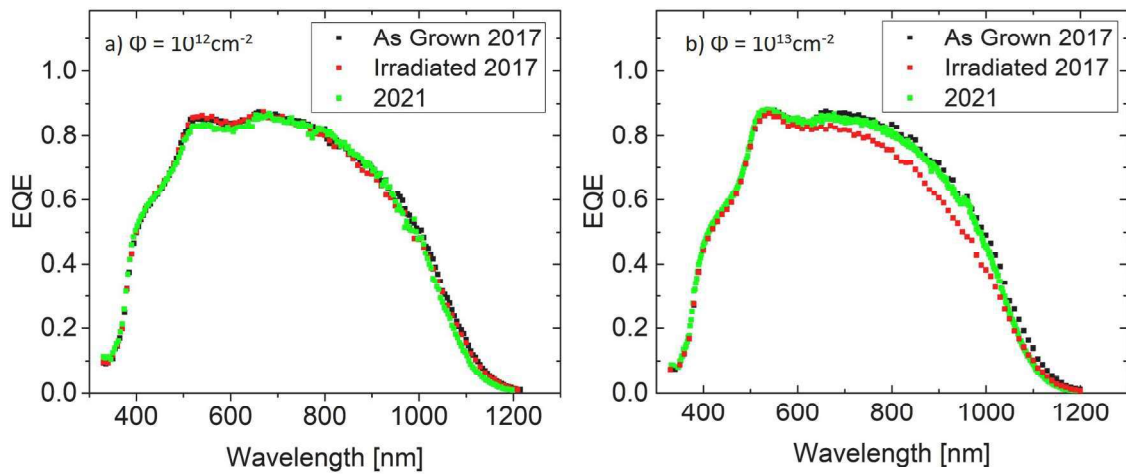


Fig. 4. The EQE response of the CZTSSe samples irradiated with proton fluences of 10^{12} cm^{-2} and 10^{13} cm^{-2} , showing no signs of significant recombination increase, or irradiation induced bandgap shift after a fluence of 10^{12} cm^{-2} , but exhibiting losses for the 10^{13} cm^{-2} case, which are subsequently recovered over time. The 2021 measurements indicate a slight widening of the bandgap compared to the as-grown samples. Figure 4b is recreated and extended through addition of new data with the permission of the authors of the initial study [5].

widening of 0.04 eV, both of which are mostly recovered over time (Fig. 4b). This appears to correspond closely to the JV curves in Fig. 3. Cu-Zn ordering is a known source of bandgap variation within CZTS(Se), however storage at room temperature seems unlikely to provide sufficient energy to induce a change in ordering of the sample that received an intermediate proton fluence, though the long time scale may play a role.

3.3. CZTS

The JV curves of the CZTS samples indicate significant radiation hardness, similar to that of CZTSSe and in fact showing a reduced V_{OC} degradation for the highest proton fluence (Fig. 5d). It is also seen that over the extended recovery period, the degradation observed in the EQE and JV of the highest fluence sample after irradiation is fully recovered, with a very slight improvement observed in the sample's EQE response (Fig. 6b). The sample irradiated with a low fluence of 10^{10} cm^{-2} was observed to show no measurable degradation for any performance parameter.

With the exception of the sample receiving a proton fluence of 10^{12} cm^{-2} it can be seen that each sample shows a gain in V_{OC} over time. No increases in the samples' bandgaps were observed and neither was a significant improvement in the EQE response (Fig. 6). An accelerated aging investigation by Neubauer, et al. [17] using 100°C air anneal also observed an increase in the V_{OC} of CZTS samples. At present, we cannot

offer an explanation for this observed increase. A PL and JV study by Sugiyama et al. reported V_{OC} degradation for proton fluences in excess of 10^{13} cm^{-2} and a considerable reduction in the intensity of the primary PL peak [6] (attributed by the authors to Cu_{Zn} , which is calculated to be the dominant p-dopant in CZTS [18]). Though no CV data from 2017 exists for the samples, measurements performed in 2021 display minimal differences in net doping between the samples (approximately $0.2 \times 10^{15} \text{ cm}^{-3}$) and each sample has a value in the range $1.0\text{--}1.5 \times 10^{16} \text{ cm}^{-3}$ which is within the regular range of expected values [19,20].

4. Summary

The long-term recovery of thin-film CIGS, CZTS and CZTSSe solar cells irradiated by 3 MeV protons was investigated through IV and EQE characterisation. It was observed that the CIGS cells recovered a significant proportion of V_{OC} which was highly degraded by irradiation (99%, 94% and 86% in order of increasing dose), whilst CZTS and CZTSSe samples retained similar V_{OC} values as were observed after two months of dark storage (in the region of 95%). Moreover, it was seen that the maximally irradiated CIGS cells exhibited much greater recombination losses than the lesser irradiated samples, showing significant EQE response degradation. This degradation in the EQE was nearly fully recovered after the extended dark storage period, however considerable V_{OC} degradation is still present. It is speculated that the V_{OC} losses are caused by deep defect states created by the irradiation and that the

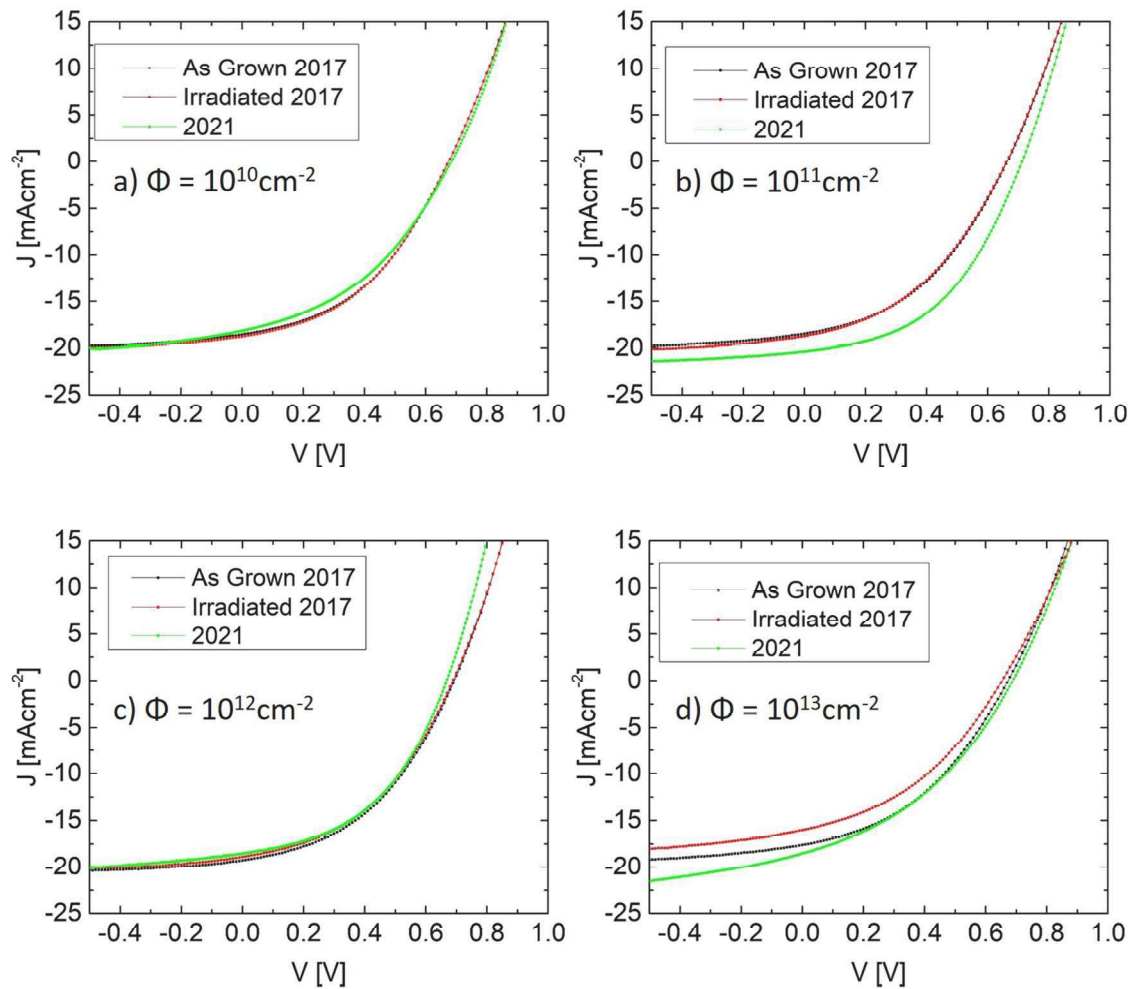


Fig. 5. JV curves of the CZTS samples, also including a sample irradiated with a proton fluence of 10^{10} cm^{-2} . The samples exhibit significant radiation hardness similar to, if not in excess of, that of CZTSSe, with no significant degradation observed for proton fluences below 10^{13} cm^{-2} and only a minor reduction in V_{OC} for this highest fluence. Figure 5d is recreated and extended through addition of new data with the permission of the authors of the initial study [5].

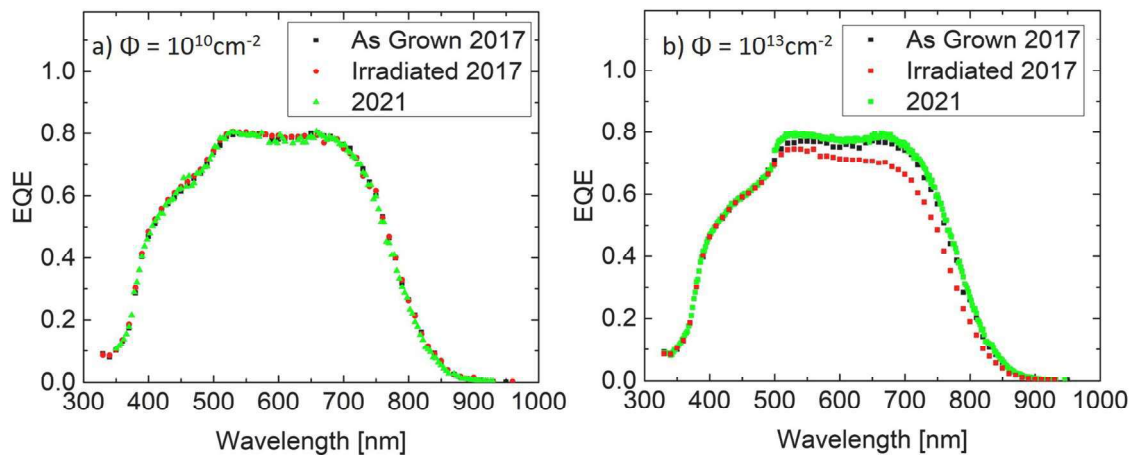


Fig. 6. The EQE response of the CZTS samples for $\Phi = 10^{10} \text{ cm}^{-2}$ and $\Phi = 10^{13} \text{ cm}^{-2}$, showing no evidence of significant radiation-induced recombination or bandgap shifting for the low fluence sample, and a full recovery of irradiation induced degradation over time for the high fluence sample. Figure 6b is recreated and extended through addition of new data with the permission of the authors of the initial study [5].

density of such defects increases significantly for high proton fluence. It is also possible that additional mechanisms could be at work, with literature sources suggesting that net doping is decreased by irradiation. It is further speculated that the CZTS and CZTSSe samples have recovered fully from the radiation induced degradation, with aging-related degradation now impacting key electrical characteristics of the CZTSSe samples. The EQE cut-off wavelength of all CZTSSe samples was observed to decrease, whilst three of the four CZTS samples were observed to gain in V_{OC} after extended dark storage. Further work is planned to investigate the observed phenomena, using photoluminescence and thermal admittance spectroscopy techniques to learn more about the radiation-induced defects, in addition to using a broader range of proton fluences to investigate the possibility of a high-damage regime fluence threshold for CZTS and CZTSSe, as was observed in the CIGS. Raman spectroscopy is also planned to be used, to investigate whether Cu-Zn ordering is responsible for the bandgap widening of CZTSSe over time.

CRedit authorship contribution statement

Patrick Pearson: Investigation, Writing – original draft, Writing – review & editing, Visualization. **Jan Keller:** Conceptualization, Writing – review & editing. **Jes Larsen:** Conceptualization, Writing – review & editing. **Volodymyr Kosyak:** Methodology, Resources, Writing – review & editing. **Charlotte Platzer-Björkman:** Resources, Writing – review & editing, Supervision.

CRedit authorship contribution statement

Patrick Pearson: Investigation, Writing – original draft, Writing – review & editing, Visualization. **Jan Keller:** Conceptualization, Writing – review & editing. **Jes Larsen:** Conceptualization, Writing – review & editing. **Volodymyr Kosyak:** Methodology, Resources, Writing – review & editing. **Charlotte Platzer-Björkman:** Resources, Writing – review & editing, Supervision.

Declaration of Competing Interest

The authors declare that they have no known competing financial interests or personal relationships that could have appeared to influence the work reported in this paper.

Acknowledgements

The authors thank Solibro AB for providing the CIGS absorber

material. Thanks are also given to Sethu Saveda Suvanam for performing initial measurements and Nils Ross for fabrication of the CZTSSe samples. There are no competing interests to declare. This work was supported by the Swedish Research Council, (grant number 2019-04793) and Swedish Energy Agency, (grant number 48479-1).

References

- [1] R.M. Burgess, W.S. Chen, W.E. Devaney, D.H. Doyle, N.P. Kim, B.J. Stanbery, Electron and proton radiation effects on GaAs and CuInSe₂ thin film solar cells, in: *Proceedings of the Photovoltaic Specialists Conference, Record of the Twentieth IEEE*, 1988.
- [2] A. Jasenek, U. Rau, Defect generation in Cu(In,Ga)Se₂ heterojunction solar cells by high-energy electron and proton irradiation, *J. Appl. Phys.* 90 (2001) 650–658.
- [3] S. Kawakita, M. Imaizumi, T. Sumita, K. Kushiya, T. Ohshima, M. Yamaguchi, S. Matsuda, S. Yoda, T. Kamiya, Super radiation tolerance of CIGS solar cells demonstrated in space by MDS-1 satellite, in: *Proceedings of the 3rd World Conference on Photovoltaic Energy Conversion 1*, 2003, pp. 693–696.
- [4] S. Kawakita, M. Imaizumi, K. Kibe, T. Ohshima, H. Itoh, S. Yoda, O. Odawara, Analysis of anomalous degradation of Cu(In,Ga)Se₂ thin-film solar cells irradiated with protons, *Jpn. J. Appl. Phys.* 46 (2007) 670.
- [5] S. Suvanam, J. Larsen, N. Ross, V. Kosyak, A. Hallen, C. Platzer Björkman, Extreme radiation hard thin film CZTSSe solar cell, *Sol. Energy Mater. Sol. Cells* 185 (2018) 16–20.
- [6] M. Sugiyama, S. Aihara, Y. Shimamune, H. Katagiri, Influence of electron and proton irradiation on the soaking and degradation of Cu₂ZnSnS₄ solar cells, *Thin Solid Films* 642 (2017) 311–315.
- [7] M.A. Sulimov, M.N. Sarychev, M.V. Yakushev, J. Marquez-Prieto, I. Forbes, V. Yu Ivanov, P.R. Edwards, A.V. Mudryi, J. Krustok, R.W. Martin, Effects of Irradiation of ZnO/CdS/Cu₂ZnSnSe₄/Mo/glass solar cells by 10 MeV electrons on photoluminescence spectra, *Mater. Sci. Semicond. Process.* 121 (2021), 105301.
- [8] J.F. Ziegler, SRIM-2003, *Nucl. Instrum. Methods Phys. Res. Sect. B Beam Interact. Mater. At.* 219–220 (2004) 1027–1036.
- [9] American Institute of Aeronautics and Astronautics, Inc., Standard, Qualification and Quality Requirements for Space Solar Cells (AIAAS111A–2014), American Institute of Aeronautics and Astronautics, Inc., Washington, DC, 2014.
- [10] I. Khatir, T.Y. Lin, T. Nakada, M. Sugiyama, Proton irradiation on cesium-fluoride-free and cesium fluoride-treated Cu(In,Ga)Se₂ solar cells and annealing effects under illumination, *Phys. Status Solidi Rapid Res. Lett.* 13 (2019), 1900519.
- [11] W.J. Lee, G. Lee, D.H. Cho, C. Kang, N. Myoung, C.S. Kee, Y.D. Chung, Ultrafast photoexcited-carrier behavior induced by hydrogen ion irradiation of a Cu(In,Ga)Se₂ thin film in the terahertz region, *IEEE Trans. Terahertz Sci. Technol.* 11 (2021).
- [12] K. Yoshida, M. Tajima, S. Kawakita, K. Sakurai, S. Niki, K. Hirose, Photoluminescence analysis of proton irradiation effects in Cu(In,Ga)Se₂ solar cells, *Jpn. J. Appl. Phys.* 47 (2008) 857.
- [13] Y. Hirose, M. Warasawa, I. Tsunoda, K. Takakura, M. Sugiyama, Effects of proton irradiation on optical and electrical properties of Cu(In,Ga)Se₂ solar cells, *Jpn. J. Appl. Phys.* 51 (2012), 111802.
- [14] J.T. Heath, J.D. Cohen, W.N. Shafarman, Bulk and metastable defects in CuIn_{1-x}Ga_xSe₂ thin films using drive-level capacitance profiling, *J. Appl. Phys.* 95 (2004) 1000.
- [15] M. Cwil, M. Igalson, P. Zabierowski, S. Siebentritt, Charge and doping distributions by capacitance profiling in solar cells, *J Appl Phys* 103 (2008), 063701.
- [16] Danaki P. Radiation hardness of thin film solar cells Dissertation, 2019.

- [17] C. Neubauer, A. Samiepour, S. Oueslati, M. Danilson, D. Meissner, Ageing of kesterite solar cells 1: degradation processes and their influence on solar cell parameters, *Thin Solid Films* 669 (2019) 595–599.
- [18] S. Chen, J.H. Yang, X.G. Gong, A. Walsh, S.H. Wei, Intrinsic point defects and complexes in the quaternary kesterite semiconductor $\text{Cu}_2\text{ZnSnS}_4$, *Phys. Rev. B* 81 (2010), 245204.
- [19] M. Grossberg, J. Krustok, C.J. Hages, D.M. Bishop, O. Gunawan, R. Scheer, S. M. Lyam, H. Hempel, S. Levenco, T. Unold, The electrical and optical properties of kesterites, *J. Phys. Energy* 1 (2019), 044002.
- [20] C. Frisk, T. Ericson, S.Y. Li, P. Szaniawski, J. Olsson, C. Platzer-Björkman, Combining strong interface recombination with bandgap narrowing and short diffusion length in $\text{Cu}_2\text{ZnSnS}_4$ device modeling, *Sol. Energy Mater. Sol. Cells* 144 (2016) 364–370.

The Effect of Absorber Stoichiometry on the Stability of Widegap (Ag,Cu)(In,Ga)Se₂ Solar Cells

Patrick Pearson,* Jan Keller, Lars Stolt, Marika Edoff, and Charlotte Platzer Björkman

(Ag,Cu)(In,Ga)Se₂ solar cells with bandgaps of ≈ 1.45 eV with a large spread in absorber stoichiometry are characterized with the intention of assessing the effect of composition on the stability of the devices. This material is observed to have a poor diffusion length, leading to very strong dependence upon the depletion region width for charge carrier collection. The depletion width is observed to depend strongly upon the stoichiometry value and shrinks significantly after an initial period of dark storage. It is also seen that the depletion width can be varied strongly through light-soaking and dry-heat treatments, with prolonged annealing leading to detrimental contraction and light soaking leading to expansion which increases current collection. The extent of depletion width variation in response to the treatments is also clearly linked to absorber stoichiometry. Consequently, the device performance, particularly the current output, exhibits a stoichiometry dependence and is considerably affected after each round of treatment. Possible causes of this behavior are discussed.

1. Introduction


Cu(In,Ga)Se₂ (CIGS) is an established thin-film photovoltaic material, with record cells reaching efficiencies of 22.6%^[1] (or 23.4% with sulfur inclusion).^[2] There are still significant improvements to be made, however. The best-performing cells have bandgaps in the region of 1.0–1.2 eV but the optimum value for a single-junction solar cell is 1.34 eV.^[3] It would also be advantageous to fabricate high-efficiency widegap CIGS devices to enable the material's use as a top cell in a tandem/multijunction device. To achieve high tandem efficiencies (in the two-terminal configuration), it is estimated that bandgaps of 1.6 and 0.9 eV would be required for top and bottom cells, respectively

(or 1.91, 1.37, and 0.93 eV, for the top, intermediate, and bottom cells in a triple-junction device).^[4] Near-maximum theoretical efficiency can be attained for top cells with bandgaps in the region 1.4–1.9 eV in a four-terminal tandem configuration.^[5] Furthermore, the increased output voltages and reduced currents of widegap devices allow solar modules with reduced resistive losses and less dead area in monolithic series connections to be manufactured. By increasing the ratio of Ga to In in the material (referred to henceforth as the GGI, $[Ga]/([Ga] + [In])$), the bandgap is also increased, primarily through an energetic increase in the conduction band minimum. However, the open-circuit voltage (V_{OC}) does not increase linearly with the bandgap.^[6,7] Currently it seems that the optimal GGI lies in the range of 0.2–0.3

with values in excess of this upper bound leading to deterioration in device performance.^[7–9] There are multiple suspected causes for the negative impact of high GGI ratios, including the formation of an unfavorable conduction band offset between the CIGS absorber and cadmium-sulfide (CdS) buffer layer;^[10,11] Cu enrichment of grain boundaries (acting either as a region of high recombination or as highly conductive shunt pathways);^[12,13] tetragonal distortion of the lattice;^[14] or the increase in the energetic depth and density of malign defects.^[9,15–17] The incorporation of silver into CIGS, substituting some of the copper atoms, is expected to be beneficial, improving the conduction band offset between the silver-alloyed CIGS (ACIGS) and the commonly used CdS buffer layer.^[18] Silver incorporation in CIGS is also observed to increase grain size^[19] and reduce the melting point of the alloy, which is expected to reduce the density of defects in the material.^[20–22]

With a clear motivation to investigate the incorporation of Ag into CIGS and the realization of high-performance widegap CIGS-based devices, we produced a large series of ACIGS cells, spanning a wide range of compositions.^[23] From this work, a compositional window of interest was identified with GGI in the range of 0.66–0.79 and a silver-to-silver-and-copper (AAC) ratio of 0.47–0.67. The upper limit of AAC was chosen to reduce the amount of ordered vacancy compounds (OVCs), forming at the rear of the absorber layer, as it had been concluded that they were detrimental to device performance, acting to block carrier transport. The devices in this region have bandgaps between 1.40 and 1.49 eV and a wide spread in I/III stoichiometry ($I/III = ([Cu] + [Ag])/([In] + [Ga])$). It has been shown that

P. Pearson, J. Keller, L. Stolt, M. Edoff, C. Platzer Björkman
Division of Solar Cell Technology
Department of Material Science
Uppsala University
Box 534, 75121 Uppsala, Sweden
E-mail: patrick.pearson@angstrom.uu.se

 The ORCID identification number(s) for the author(s) of this article can be found under <https://doi.org/10.1002/pssb.202200104>.

© 2022 The Authors. physica status solidi (b) basic solid state physics published by Wiley-VCH GmbH. This is an open access article under the terms of the Creative Commons Attribution-NonCommercial-NoDerivs License, which permits use and distribution in any medium, provided the original work is properly cited, the use is non-commercial and no modifications or adaptations are made.

DOI: 10.1002/pssb.202200104

OVCs form extensively for largely off-stoichiometric samples with AAC and GGI larger than 0.5.^[22] In our previous work, the majority of OVCs were identified to be of the 1:3:5 phase, that is, (Ag,Cu)(In,Ga)₃Se₅. This phase has a bandgap approaching 2 eV^[23] and is expected to have both conduction and valence band edges significantly below those of the 1:1:2 phase.^[24] These factors combined with proximity to the front surface indicate that OVC patches are likely to effectively capture electrons and block carrier collection. It was also observed that Na accumulates in OVCs preferentially to the 1:1:2 phase, which is expected to explain why the presence of OVCs at the rear of the absorber leads to blocking, as the Na reduction in the bulk compromises the MoSe₂/ACIGS interface. In this work we investigate the stability of a smaller subsection of the previous sample set, with a narrower spread in composition and bandgap (1.44–1.47 eV; $0.71 \leq \text{GGI} \leq 0.77$; $0.54 \leq \text{AAC} \leq 0.63$; $0.79 \leq \text{I/III} \leq 0.98$). The narrow spread in AAC and GGI, in comparison with I/III stoichiometry, allows us to focus on the role of the latter parameter in device stability and in the device response to heat and light treatments. By investigating the role of I/III stoichiometry on device stability, we aim also to indirectly probe the effect of OVCs near the front surface of the absorber layer. Overall, six runs each containing four samples (with individual compositions) were analyzed, with some samples excluded due to a high number of dead or shunted cells, leading to a total of 21 samples being characterized.

2. Results

Here we present the external quantum efficiency (EQE) responses and capacitance–voltage (CV) profiles of selected representative cells from across the compositional range, split across two subsections, one detailing the effects of storage and annealing and the other the effects of light soaking (LS). In addition, the evolution of key current–voltage (*I*–*V*) performance parameters after treatment, dependent on stoichiometry, is shown for the whole sample set in the storage and annealing section. The second section displays the evolution of *V*_{OC} with prolonged illumination, showing how the changes induced by LS treatment occur very rapidly. A third section highlights the significance of depletion width in carrier collection. We emphasize now that treatments were performed in sequence, without bringing the samples into a reference state in between (pretests indicate no impact of aging and annealing on the response to LS treatments, while LS is observed to induce permanent doping changes. See Figure S9–S11, Supporting Information). Hence, the differences in performance characteristics discussed in the following sections refer to the difference compared with the values measured after the preceding treatment.

2.1. Effects of Dark Storage and Annealing

Consideration of the EQE responses for four representative cells from across the stoichiometry range (Figure 1) indicates that all

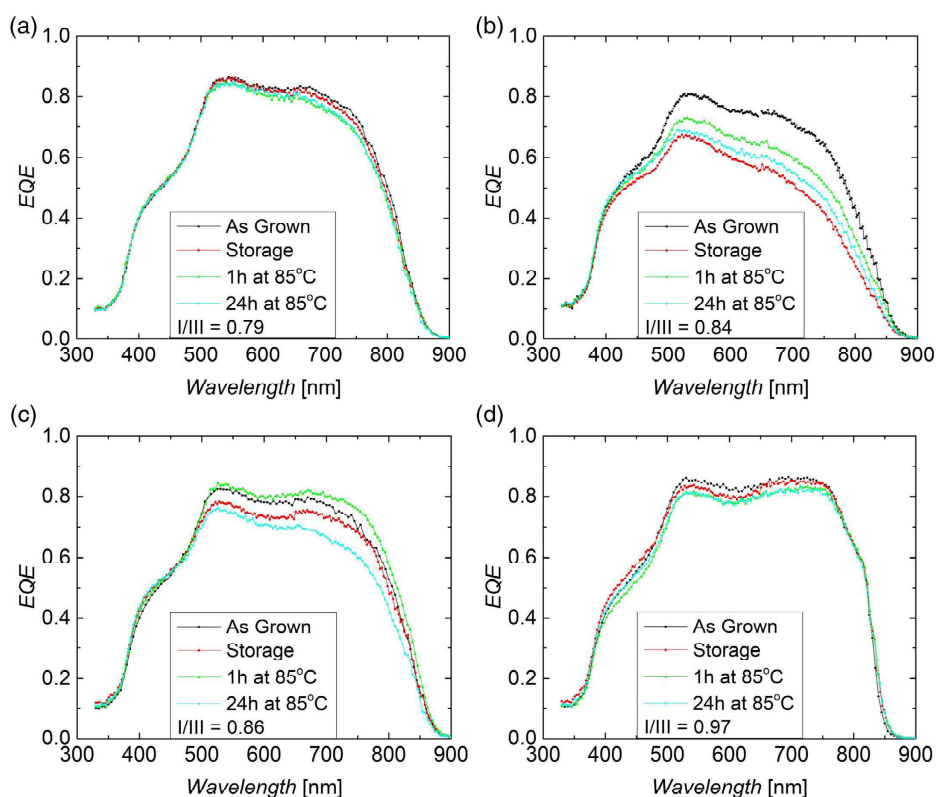


Figure 1. Evolution of EQE response for four different stoichiometries after extended dark storage, a 1 h anneal at 85 °C, and a subsequent 24 h anneal at 85 °C. It can be observed that for extremes of stoichiometry, the treatments have only a small effect on the EQE response, but for samples which are moderately off-stoichiometric, treatment-induced changes are much more severe.

cells exhibit a degraded response after extended dark storage, with a resulting loss in J_{SC} . Those cells at the stoichiometric extremes have much less degraded EQE responses. A 1 h anneal at 85 °C is seen to be beneficial for moderately off-stoichiometric devices, with significant improvement in the EQE response across all wavelengths and particularly the long-wavelength regime. Surprisingly, an extended anneal for 24 h at the same temperature was observed to cause a reduction in the EQE response, particularly in the long-wavelength regime, indicating a loss in carrier collection, due either to a reduction in depletion width or to diffusion length.

The effect on the EQE response of storage and heat treatments is mirrored in the doping profiles extracted for the same representative devices (**Figure 2**). A 1 h anneal is observed to significantly expand the depletion width of all cells (all but the least off-stoichiometric sample see increases approaching 100%). A 24 h anneal is then observed to contract the depletion width, particularly for the moderately off-stoichiometric samples, with the reduction exceeding the gain from a single hour in both cases. It was suggested in a previous work^[25] that the widegap ACIGS devices have a very poor diffusion length and so exhibit highly depletion-dependent carrier collection. This conclusion is verified by our results, also explaining the minimal shift in the EQE response for samples at the extremes of the stoichiometry range as they are already so heavily depleted, that even considerable contraction or expansion does not significantly affect the collection efficiency in the device, whereas for the narrowly depleted

moderately off-stoichiometric samples, minor changes in depletion can cause significant changes in the collection profile. About three months after initial fabrication, a small number of devices were characterized with C–V measurements. A comparison of the depletion widths measured at this time, with regard to the stoichiometry value, indicates that the EQE degradation during the extended dark storage is also likely to stem from the depletion zone contraction, following the responses to annealing (see Figure S1 in the supporting information for more information).

Figure 3a displays the depletion width extracted for each sample, revealing the dependence on I/III. Moreover, through consideration of **Figure 3b**, it can be seen that those trends observed for the four representative cells are upheld throughout the whole sample set and compositional range. The depletion widths of moderately off-stoichiometric samples are shown to expand after a 1 h anneal, whilst very off- and close-stoichiometric samples do not exhibit significant variation, with the exception of the two most off-stoichiometric samples (I/III = 0.79, 0.81). The subsequent contraction of the depletion width after the 24 h hour anneal also follows such an arch shape. A simple explanation for the dependence of depletion width on stoichiometry, close to stoichiometry, is that there is a decreasing density of group-I vacancies (V_I) toward stoichiometric composition, reducing the net doping. For very off-stoichiometric material, the increase in depletion width is unexpected, as an increase in V_I should increase the acceptor concentration in the material.

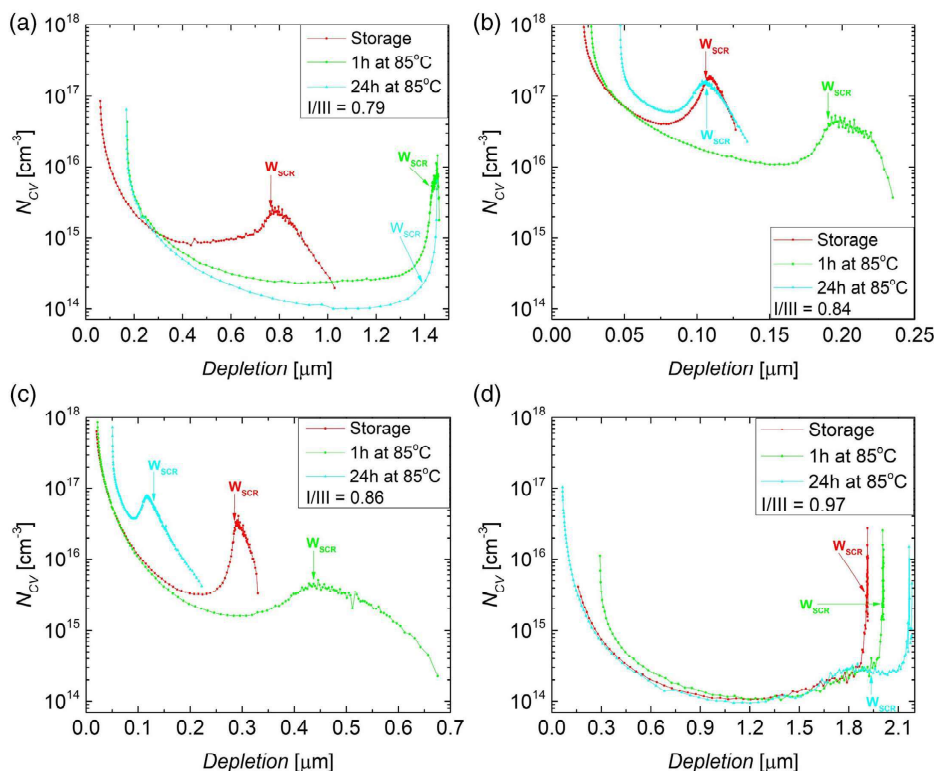


Figure 2. Evolution of the doping profiles of four different stoichiometries after extended dark storage, a 1 h anneal at 85 °C and a 24 h anneal at 85 °C. It can be seen that the shifts observed in the depletion width at zero bias after treatments are related to the shifts in EQE response after treatment (**Figure 1**), with contraction of the depletion region leading to a reduction in the longer-wavelength EQE response. It can also be seen that devices that are very off-stoichiometric have very wide depletion regions, while close-stoichiometric devices are even fully depleted (note the significant difference in x-scales).

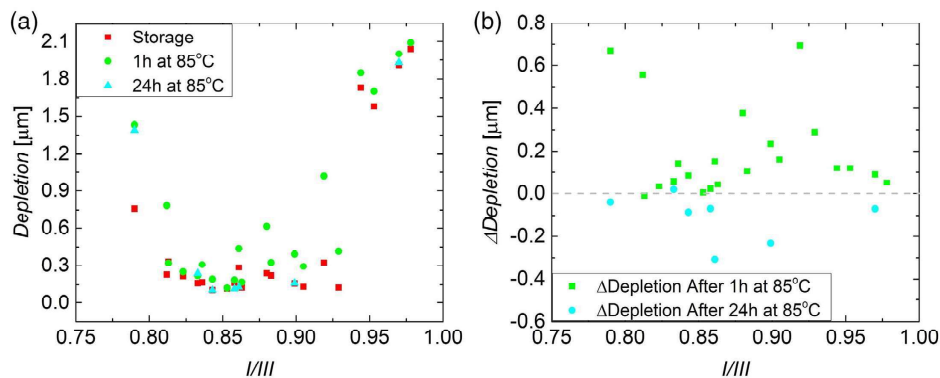


Figure 3. a) The observed dependence of zero-bias depletion width on sample stoichiometry, for all samples, after each round of treatment. Note that for the extremes of the stoichiometry range ($I/III \lesssim 0.8$, $I/III \gtrsim 0.95$), depletion is large, reducing significantly in the intermediate region. b) This plot shows how a 1 h anneal leads to a general expansion of the zero-bias depletion width, while the 24 h hour anneal leads to contraction. Both responses follow a similar arch-shaped trend, with relation to stoichiometry.

For such extreme off-stoichiometry, however, the OVC fraction is significant and it is possible that the 1:1:2 phase itself begins to alter. Such dramatic changes to the material system could lead to the observed wide depletion. In addition, as the material becomes increasingly group-I poor, the density of group-III anti-site defects is likely to increase. In/Ga_{Cu} are known donor-type defects in CIGS and the similar radii of In, Ga, and Ag could lead to the formation of In/Ga_{Ag} being more favorable than their Cu counterparts, reducing the net-doping level and expanding the depletion region. This self-compensation is, however, always present in CIGS, so it would be unexpected for the level of self-compensation to become dramatically more pronounced below $I/III \approx 0.80$.

Turning to the I - V parameters (Figure 4), it is seen that there is a slight degradation in V_{OC} after the storage period, with increasing degradation for increasing I/III (Figure 4b). The 1 h anneal is observed to have no clear effect on V_{OC} ; however, the 24 h anneal appears to have a beneficial effect on close-stoichiometric samples ($I/III \geq 0.90$). The response of J_{SC} to each treatment is observed to follow an arch trend, with respect to stoichiometry, with response minima for extremely off- or close-stoichiometric values and the maximum shift at an intermediate value of $I/III \approx 0.87$ (Figure 4b). This arched dependence on stoichiometry is clearly connected to that of the depletion width seen in Figure 3b. The extended dark storage leads to very significant degradation in J_{SC} (up to 8 mA cm^{-2});

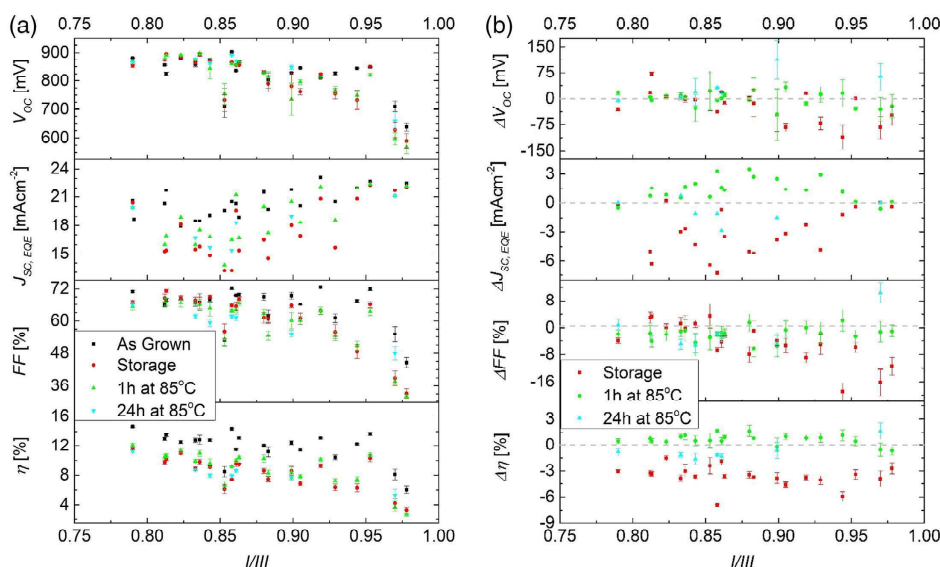


Figure 4. a) Dependence of key I - V performance parameters on stoichiometry for samples as grown, after extended dark storage, and after annealing at 85 °C. b) Dependence of the change in the I - V parameters measured after treatments, on stoichiometry. A clear positive correlation between FF losses over time and stoichiometry can be seen, in addition to a clear stoichiometry-dependent trend for J_{SC} response to treatment, with moderately off-stoichiometric devices being the most responsive. Error bars define the standard error across the samples and data points represent sample averages. As J_{SC} is extracted from single EQE measurements on representative cells, no error bars are given.

however, the short anneal results in partial recovery (gaining up to 4 mA cm^{-2}). In line with the $C-V$ and EQE measurements, the 24 h anneal led instead to further reductions in J_{SC} (peak loss of $\approx 3 \text{ mA cm}^{-2}$). FF was observed to degrade over time, with a clear correlation between stoichiometry and the severity of the degradation. Both anneals led to a slight decrease in FF, but no trend coupling degradation to stoichiometry was observed. It appears that η is led by V_{OC} and FF for close-stoichiometric samples, while the off-stoichiometric samples are led by variations in J_{SC} . After the storage period, a fairly uniform and significant degradation of $\approx 3\%$ absolute is observed, with slightly greater degradation for samples closer to stoichiometry (presumably stemming from the increased FF and V_{OC} degradation in this compositional region). Following the 1 h anneal, η displays a slight recovery (0.5–1.0%) for all samples with stoichiometry below 0.95, and these close-stoichiometric samples instead exhibit a further degradation of $\approx 1\%$. After the 24 h anneal, a positive correlation between stoichiometry and recovery can be observed for η , presumably stemming from the similar trend observed for V_{OC} .

2.2. Effects of LS

As with the response to storage and heat treatments, it can be seen in **Figure 5** that devices within the intermediate stoichiometry range have greater responses to LS than those at the extremes of the range, which are affected only very little (the severely off-stoichiometric sample exhibits small gains in

the long-wavelength region, and the close-stoichiometric sample instead exhibits a very minor loss). It can be noted that the extremely off-stoichiometric sample ($I/III = 0.79$, **Figure 5**) is subjected to LS, in addition to having previously been annealed for 24 h. This was deemed as acceptable due to the almost non-existent effect of the extended anneal on the device's EQE and $C-V$ responses (the latter in **Figure 6a**). Moreover, the threshold between the extremely and moderately off-stoichiometric effects seems to be at $I/III \approx 0.80$, so it was necessary to reuse the sample. Interestingly, the sample with $I/III = 0.88$, which for heating and storage effects can be considered to lie well within the “moderate” range, shows a much reduced response to LS (**Figure 5c**), compared with the device with $I/III = 0.84$ (**Figure 5b**). This may be explained by a comparison of the doping profiles of the two samples (**Figure 6b,c**). Through consideration of the absorption profile of the material, it can be estimated that $\approx 90\%$ of generation occurs in the first $\approx 1 \mu\text{m}$ of the absorber material.^[25] Due to the poor diffusion length in the material, it can be expected that the carrier collection profile shrinks to zero very quickly for depths outside of the depletion region. Thus, we can expect that for samples with depletion widths $\leq 1 \mu\text{m}$, expansion of the depletion region is highly beneficial and will improve collection efficiency significantly; however, further expansion of depletion beyond $1 \mu\text{m}$ is unlikely to yield significant improvements. With this in mind, we return to the doping profiles of the two samples. Prior to LS, they had depletion widths of ≈ 0.3 and $\approx 0.6 \mu\text{m}$ for I/III of 0.84 and 0.88, respectively. After

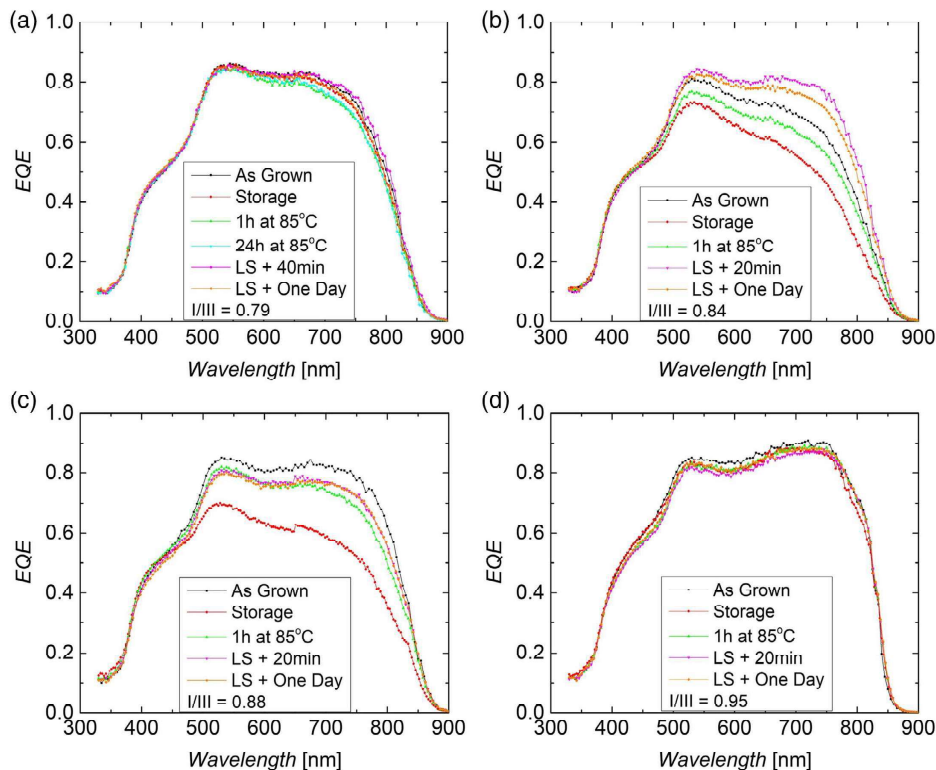


Figure 5. Evolution of EQE response for four different stoichiometries after extended dark storage, a 1 h anneal at 85°C and 7 h of LS (for $I/III = 0.84$, 0.88 , and 0.95), or 5 h of LS ($I/III = 0.79$). Again it can be noted that the moderately off-stoichiometric samples respond much more to treatment than those at the extremes of the stoichiometric range.

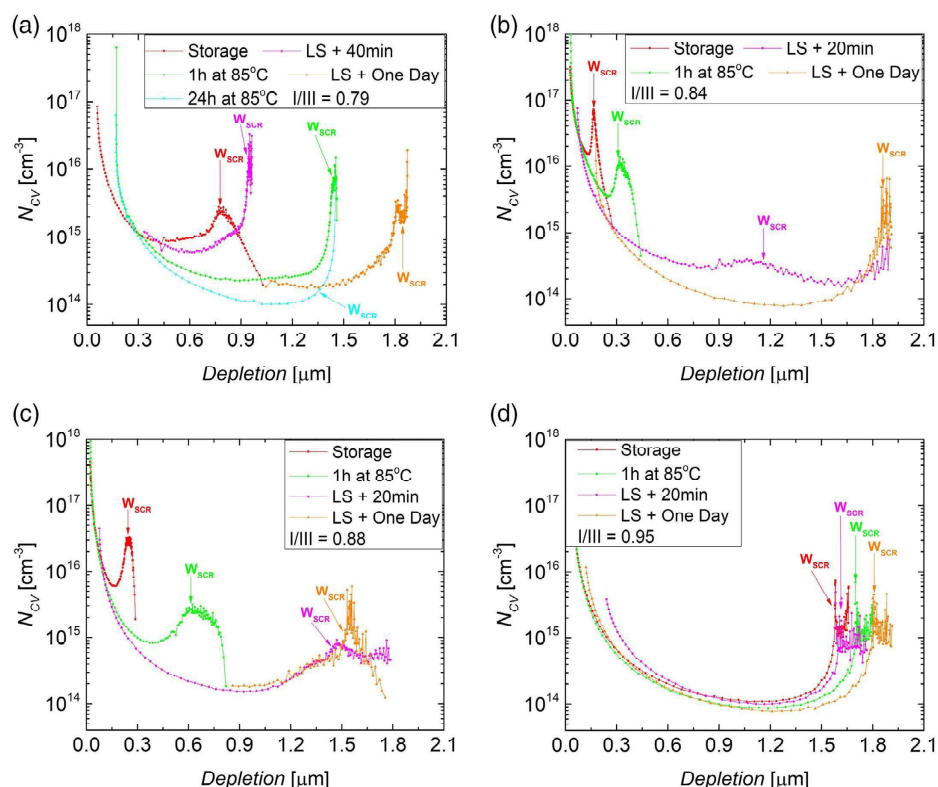


Figure 6. Evolution of the doping profile for four different stoichiometries after extended dark storage, a 1 h anneal at 85 °C, and 7 h of LS (for $I/III = 0.84$, 0.88 , and 0.95) or 5 h of LS ($I/III = 0.79$). Interestingly it is observed that while the intermediate samples see significant expansion of the depletion region, those at the extremes of the stoichiometric range actually see contraction, particularly the sample with $I/III = 0.79$.

LS, both samples have depletion regions extending beyond 1 μm . With the improvement limitation we have just established, we see that the sample with $I/III = 0.84$ had a much greater capacity to improve collection; hence, we observe much greater improvement, despite similar final depletion widths.

It is observed in Figure 6 that for extremely off-stoichiometric devices, the depletion region is significantly contracted (shrinking by more than 0.3 μm), despite also being observed to exhibit improvements in collection (Figure 5). It is suggested that the device is still sufficiently depleted to avoid collection losses from depletion width contraction. Likewise, the close-stoichiometric sample showed a small depletion width contraction but no significant variation in current collection. The samples were measured again, one day after LS. The sample with $I/III = 0.84$ was observed to lose some collection in the longer wavelengths, while the other sample's responses remained unchanged. This is an unanticipated result, as $C-V$ measurements performed the day after LS reveal that the depletion region of that sample expanded further. Due to the already considerable depletion, we would expect no, or a very slight positive, change to the EQE response. This was the case for the other three samples, wherein each exhibited expansion of the depletion region. The evolution of the depletion width after one day does not appear to show relaxation of the changes induced by LS treatment, as there is no simple reversion of changes (complete or partial).

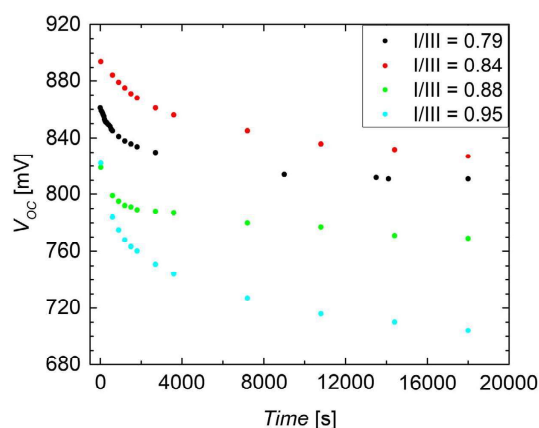


Figure 7. Evolution of the V_{OC} of four devices with different stoichiometries during 5 h of LS. A clear decay in V_{OC} can be observed and we speculate that the main effect occurs up to a time of 4000 s, before temperature effects prevent a final saturation of V_{OC} .

By tracking the evolution of key $I-V$ performance parameters over LS (Figure 7 and Table 1), it was observed that the most significant changes in performance occur within the first 4000 s of LS. V_{OC} is observed to decay steeply within the initial time period, with losses increasing with stoichiometry (35, 50,

Table 1. Evolution of I – V performance parameters over time under AM1.5 illumination. Note the dramatic change in the first 2700 s, followed by more gradual evolution (no measurements were taken near the 4000 s saturation point).

I/III	Time [s]	V_{OC} [mV]	J_{SC} [mA cm ^{−2}]	FF [%]	η [%]
0.79	30	859	19.9	67.2	11.5
	2700	830	21.1	66.1	11.6
	18 000	811	21.4	63.3	11.0
0.84	30	894	17.1	56.9	8.7
	2700	861	19.5	67.1	11.3
	18 000	827	21.1	62.0	10.8
0.88	30	819	14.65	59.4	7.1
	2700	788	14.8	60.8	7.1
	18 000	769	15.5	59.9	7.1
0.95	30	822	20.2	63.2	10.5
	2700	751	20.0	61.6	9.3
	18 000	704	20.0	57.7	8.1

75, and 125 mV for I/III of 0.79, 0.84, 0.88, and 0.95, respectively). After this initial decay, it is believed that the gradual degradation in the V_{OC} is due to increasing device temperature (although a Peltier element is used to cool the device during illumination, this system is not perfect, with samples heating from ≈ 295 to ≈ 305 K over the illumination period). By performing an I – V measurement 20 min after LS, it was observed that the performance parameters all recovered toward their values at the end of the initial period of rapid change, verifying our suspicion. The highly off-stoichiometric devices (I/III = 0.79 and 0.84) exhibit a steep increase in J_{SC} , which plateaus at the end of the initial 4000 s period, with subsequent low-level gains attributed to temperature effects. The moderately off-stoichiometric sample (I/III = 0.88) shows very minimal improvements in J_{SC} and the close-stoichiometric sample (I/III = 0.95) showed no J_{SC} gains or losses. Unexpectedly, a considerable discrepancy between the EQE and I – V results is noted here, with the EQE response of the extremely off-stoichiometric sample showing only a minor increase and the measured J_{SC} for the intermediate sample I/III = 0.88 being ≈ 5 mA cm^{−2} greater for EQE than I – V (Table 1). Due to the calibration of the I – V setup, a slight underestimate of J_{SC} is expected for I – V measurements, compared with EQE; however, none of such magnitude was observed previously in this sample set. Interestingly, the discrepancy between the I – V and EQE values of J_{SC} was observed to broaden after each treatment (see Figure S5, Supporting Information); however, an explanation for this cannot be provided. The FF and efficiency of the two moderately off-stoichiometric samples were observed to follow J_{SC} evolution, until the plateau was reached, whereupon V_{OC} reduction could be seen to reduce these figures of merit. The FF and efficiency of the samples at the extremes of the compositional range were observed to be led strongly by V_{OC} .

These results are interesting, as they show a departure from the pattern observed for annealing, of an intermediate “active” stoichiometry region ($0.8 \leq I/III \leq 0.9$), which is highly

responsive to treatment and two unresponsive regions outside the bounds of the intermediate, though the changes in the close-stoichiometric sample mirror those seen after extended dark storage. In the case of V_{OC} , there is a clear direct dependence on stoichiometry, while J_{SC} appears to be more responsive for moderate-to-extremely off-stoichiometric samples and unresponsive for moderately off- to close-stoichiometric samples. This could indicate an alternative mechanism to that driving the changes observed after annealing and storage. The apparent mismatch between J_{SC} gain and depletion evolution for the samples with I/III of 0.79 and 0.88 is attributed to the previously discussed assumption of a maximum beneficial depletion width, beyond which no collection gains are made.

2.3. Effect of Depletion Width on Carrier Collection

Figure 8 shows the extent to which J_{SC} depends on the width of the depletion region, with a clear saturation of improvement once the width of $\approx 1 \mu\text{m}$ is reached. It is expected that this depth is needed to absorb the vast majority of incident photons. Indeed this is supported by calculation and absorption measurements made by our group previously for the larger sample set.^[25] It can also be seen that by extending the depletion width from 100 to 400 nm, a significant improvement (greater than 50%) in J_{SC} can be delivered. The curves represent J_{SC} values deduced from EQE curves calculated from the generation profile and collection efficiencies, for different depletion width values, assuming a diffusion length of 300 nm, an absorber thickness of $2.0 \mu\text{m}$, and a rear-surface recombination velocity of 10^7 cm^{-1} . The collection function was derived from the study by Green et al.^[26] and the absorption coefficients were determined using a function adjusted to match previous measurement data (of ungraded representative devices with a bandgap of 1.47 eV); reflection values were also taken from a previously measured

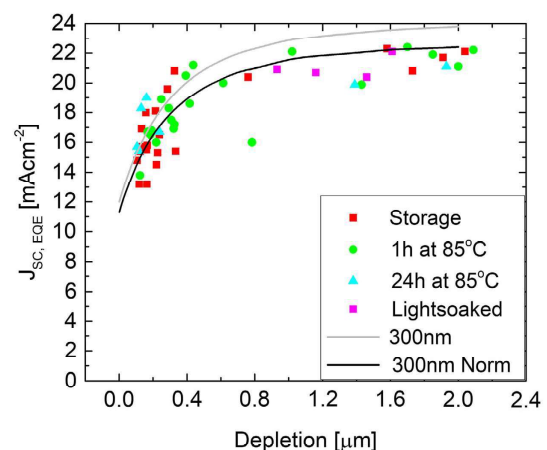


Figure 8. Dependence of J_{SC} (from EQE) on W_{SCR} . The depletion-dependent collection is clear to see from the very steep gradient for $0.0 \leq \text{depletion width} \leq 0.4 \mu\text{m}$ and it appears that our earlier estimate of $1.0 \mu\text{m}$ marking the threshold, beyond which the extension of the depletion region yields little gain, was justified. Calculated EQE responses for similar devices with a bandgap of 1.47 eV and a diffusion length of 300 nm yield a similar trend.

device. The calculated data were normalized to the maximum measured J_{SC} (from EQE) to account for overestimation attributed to differences in reflection and grading between our devices and the reference. It can be seen that the normalized curve is a relatively good fit, confirming that the diffusion length in widegap ACIGS absorbers is indeed rather low (≈ 300 nm). The absorption data and corresponding simulated EQE spectra can be found in the (Figure S6 and S7, Supporting Information).

3. Discussion

As summarized in Table 2, there is a complex interconnection between absorber stoichiometry, applied treatment, and resulting change in I - V parameters. It is, however, clear that the primary driving force for change in performance is the varying doping level/depletion width, but the mechanism that drives this variation is not clear. Moreover, it is unclear how the V_{OC} of moderately and extremely off-stoichiometric devices has relatively small variations, despite considerable increases and decreases in the net doping levels after annealing and storage. Another surprising result is that the effects of a 1 and 24 h anneal are opposing, with the former leading to expanded depletion widths and an improvement in collection, and the latter yielding the reverse both with little-to-no impact on V_{OC} . Figure 8 indicates that the active region of the ACIGS absorbers extends to ≈ 1 μ m, that is, current contribution beyond this depth is negligible. Considering the importance of the first 1000 nm, a layer of several hundred nanometers at the surface could have a significant impact on device performance, but as no such surface layer has been observed for the samples, it is likely that the mechanism driving the effects that we observe is a bulk effect. This suggests

Table 2. Summary of treatment effect on I - V performance parameters for extremely (Ex), moderately- (Mod) and close- (Sto) stoichiometric samples. – indicates that there was no clear trend after treatment, \uparrow indicates an improvement, and \downarrow indicates a loss. Paired arrows indicate a severe improvement/loss.

	I/III	Dark Storage	1 h Anneal	24 h Anneal	LS
V_{OC}	Ex	–	–	–	\downarrow
	Mod	–	–	–	\downarrow
	Sto	\downarrow	–	\uparrow	$\downarrow\downarrow$
J_{SC}	Ex	–	–	–	\uparrow
	Mod	$\downarrow\downarrow$	\uparrow	\downarrow	$\uparrow\uparrow$
	Sto	–	–	–	–
FF	Ex	–	–	–	\downarrow
	Mod	–	–	–	\uparrow
	Sto	$\downarrow\downarrow$	–	–	\downarrow
η	Ex	\downarrow	–	\downarrow	\downarrow
	Mod	\downarrow	–	\downarrow	\uparrow
	Sto	\downarrow	–	\downarrow	\downarrow
Depletion	Ex	NA	$\uparrow\uparrow$	–	$\downarrow\downarrow$
	Mod	NA	$\uparrow\uparrow$	$\downarrow\downarrow$	$\uparrow\uparrow$
	Sto	NA	\uparrow	–	\downarrow

that OVCs do not play a dominant role in what we observe, as they are closely confined to the surface for all but the most off-stoichiometric samples.^[23] In order to explain the observed behaviors, we can consider several mechanisms: Mobile ion-driven mechanisms, mechanisms relating to phase stability and segregation, and defect-driven mechanisms. We shall first consider the potential role of mobile ions in our material system.

The possible candidates for ionic diffusion are Na, Cu, and Ag, with all three being highly mobile within the material.^[27–30] A selection of samples from across the compositional range were measured with glow-discharge optical emission spectroscopy (GDOES) before and after the 1 h anneal, in order to observe any changes in the elemental distribution (see Figure S2, Supporting Information). The resulting measurements gave no clear indication of ionic redistribution after annealing; however, it is to be noted that this technique provides a laterally integrating depth profile of the elemental distribution, so this result does not rule out diffusion of ions in or out of the grain boundaries (GB) or OVCs. Considering the similar behavior of highly off-stoichiometric and close-stoichiometric samples, it appears that OVCs do not play a key role in the mechanism of depletion width modification that we observe. Consequently, as OVCs have been seen to accumulate large quantities of Na,^[23] it also seems unlikely that Na plays a critical role in the processes observed. In order to fully exclude Na migration, devices with Na-free substrates, or substrates containing heavier alkalis will be manufactured in the future, and similar experiments performed.

A possible explanation for the contrasting results of a 1 h and 24 h anneal could be that there is a maximum amount of ion migration that proves to be beneficial for device performance, with an optimum point that, when passed, leads instead to a negative effect on performance. Raghuwanshi, et al. showed that in CIGS, benign GBs are Cu depleted and malign GBs are Cu-rich and contain oxygen.^[13] Thus it could be that through annealing, the Cu content of GB is changed and oxygen given a passage into the absorber. Indeed, the devices investigated were not encapsulated, so the ingress of atmospheric elements is a possibility and could have been aggravated through annealing. GDOES data again indicate that this is not the case, with no discernible change in oxygen content after annealing (see Figure S4 and S5, Supporting Information). Deitz et al. also observed clustering of deep defects around certain GBs in ACIGS, with the defect region Cu rich and with sulfur suspected to diffuse from CdS and substitute Se.^[31] The long anneal could cause Cu enrichment and diffusion of undesirable elements into GBs. Ag, In, and Ga have very similar ionic radii, so the diffusion of Ag could lead to antisite defects.^[19] Although OVCs have been deemed rather unlikely to trigger the depletion width variation, it is to be noted that even for nearly full absorber depletion, highly off-stoichiometric devices never attain EQE spectra as high as those of the close-stoichiometric devices, indicating that there is perhaps a reduction in carrier collection caused by OVCs that operate in parallel with the main observed effects.

We now turn to consider the role of phase stability. Sopiha, et al. indicate that the thermodynamic stability of our compositional window is low, even at 50 °C, indicating that phase separation could begin at our annealing temperature of 85 °C.^[32] At such low temperatures, however, this effect would be slow and present on the nanoscale, rather than causing the large

macroscale changes in performance that we see. Varying GGI and AAC ratios throughout the material would effect the phase separation probability and temperature threshold. However, the kinetics would still be too slow in the investigated temperature range for any phase to degrade so severely and so quickly. Moreover, phase decomposition would be irreversible; however, we observe that partial recovery can be achieved.

Finally we consider the presence of metastable defects, starting with the well-known Lany–Zunger (LZ) model, which explains how the ($V_{\text{Se}} - V_{\text{Cu}}$) divacancy complex mediates the improvement of device performance after LS and deterioration following dark storage and/or annealing.^[33] It is claimed that the divacancy complex has two configurations, one acting as a donor and the other as an acceptor (paired with a deep defect). Illumination enables the conversion of donor-type configurations to acceptor-type configurations, leading to an increase in V_{OC} , while dark annealing leads to relaxation from acceptor- to donor-type configurations. Experimental works using ACIGS devices with much lower Ag and Ga content than here (≤ 0.2 and 0.4 , respectively) appear to be consistent with this theory.^[34,35] Erslev, et al. investigated LS effects on ACIGS using a broader range of Ag and Ga compositions ($0.16 \leq \text{AAC} \leq 0.76$ and $0.29 \leq \text{GGI} \leq 0.83$) and also yielded results consistent with LZ theory.^[7] Our results are not consistent with the predictions of the LZ theory, at least not those made for ACIGS with much lower Ag and Ga content. It is possible that for much higher Ga and Ag contents than originally considered in the theoretical work, the equilibrium distribution of divacancy configurations is much more acceptor rich (through shifting of the Fermi level), and the barrier to transition to the donor configuration reduces, meaning that upon LS, there is a transition to a donor-type-dominated configuration space. This could then correspond to dark annealing increasing the acceptor-type configuration population, also increasing the deep defect density, and explaining the shrinking depletion width and stable V_{OC} after the prolonged anneal (two parallel yet opposing effects).

Alternatively, we may not have such a defect playing a critical role, but rather another form of the photoactivated barrier, like Czudek, et al. discussed with connection to the persistent photoconductivity effect in CIGS,^[36] or metastable defect, such as a DX state (possibly $\text{In}/\text{Ga}_{\text{Cu}}$),^[16,37] that is activated or somehow transformed between states through LS and annealing. Indeed, a significant trap state located at $E_{\text{V}} + 0.59$ eV and attributed to $\text{Cu}_{\text{In}}/\text{Ga}$ has been observed in several studies and seen to reduce after annealing, perhaps through reduction of disorder in the material.^[31,34] Igalson et al. investigated the dependence of metastable effects on absorber composition and found that for CIGS absorber stoichiometry between 0.8 and ≈ 0.9 , the typical metastable defect concentration exceeded 10^{17} cm^{-3} .^[38] This range matches our most reactive compositional region. Unfortunately, there is a dearth of theoretical work dealing with the defect nature of high-Ga, high-Ag ACIGS material, so further experimental and theoretical studies are needed for a more comprehensive understanding.

4. Conclusion

To conclude, ACIGS samples with a narrow range of AAC and GGI values, but with a large spread in I/III stoichiometry, were

characterized using I – V , EQE, and C – V measurements to investigate their stability with respect to time, heat, and light. It was determined that the key parameter for the material is the doping and corresponding width of the depletion region. Variations in these parameters are seemingly responsible for all other parameter changes that are observed, due mainly to the very low diffusion length in the material. The ease with which the depletion width can be manipulated suggests that treatment-induced performance changes are at least partially reversible, though due to uncertainty surrounding the driving mechanism of the observed changes, it cannot be claimed that these fundamental changes are reversed, in contrast to simply layering opposing effects. Furthermore, as the age, light, and extended annealing treatments led to severe deterioration of output current and voltage, the suitability of this material for real implementation in the field is questionable, unless the degradation can be somehow mitigated. A second issue that became evident in the course of this work is the lack of theoretical investigation into high-Ag and/or high-Ga (A)CIGS devices, particularly with respect to defect theory.

This work leaves several open questions; first among these is what mechanism is acting to change the doping and depletion width after the treatments? The primary candidates are ion migration around GB and/or the presence of an undefined metastable defect state. Second, the symmetry between close- and very off-stoichiometric material (for annealing and storage responses) is surprising, though it does indicate that OVCs are not the culprit. Third, why do the 1 and 24 h anneals have opposite effects (and of similar magnitude)? A fourth point of interest is to identify whether there is in fact a different mechanism mediating the responses to annealing and LS treatments, as perhaps indicated by relating responses to stoichiometry. Finally, the limited response of V_{OC} of off-stoichiometric devices to considerable changes in doping and depletion caused by extended storage and annealing remains unclear. These questions require the support of theoretical studies to answer, in addition to further experiments to probe the defect character of the material.

5. Experimental Section

The devices were characterized by I – V , EQE and C – V measurements. I – V and EQE measurements were performed using home-built setups, the former used an ELH lamp for illumination and a water-cooled Peltier element to keep the cell temperatures at 25°C . C – V measurements were performed with an Agilent 4284A Precision LCR Meter and Keithley 2401 Source Meter. The C – V measurement sweep frequency was determined via admittance measurements, using the frequency that brought the phase angle closest to 90° (≈ 60 kHz, for all devices, see Figure S12 and S13, Supporting Information for example data). Voltage bias was swept from -0.5 V to a value near the individual cell's V_{OC} values (about 0.9 V for most cells). The material permittivity was taken to be 10 , as our previous work revealed that a value of 12 was too large.^[25] Some cells were also studied with GDOES using a Spectra Analytik GDA 750 HR system.

Each ACIGS processing run involved four samples, placed such that there was a lateral I/III stoichiometry grading, due to the arrangement of the elemental sources. The I/III variation across the run was $\approx 10\%$, with much smaller variations in GGI and AAC ($\approx 3\%$ for each). For further details, we refer the reader to the study by Keller et al.^[25] The devices were fabricated in January, February, and March of 2021, with initial measurements performed at that time. Subsequent measurements were performed in July 2021 to evaluate the effects of aging on the cells after

roughly half a year of dark storage. After these measurements, all samples underwent a dry anneal at 85 °C for 1 h. Then the samples were divided into two groups, one receiving a 24 h dry anneal at 85 °C and the other being light soaked for 7 h under approximate AM1.5 illumination and cooled via the Peltier element built into the sample stage. One sample, with a stoichiometry value of 0.79, underwent both the 24 h hour anneal and a 5 h LS. It is important to highlight that the treatments were performed in sequence, with no reference state established or referred to (see the supporting information for more details).

Each device comprised a stack of the following layers: soda lime glass (SLG)/Mo/NaF/ACIGS/CdS/*i*-ZnO/ZnO:Al. The Mo back electrode was sputtered (DC) on the glass substrates and NaF (10–15 nm) was then evaporated on top. No alkali diffusion barrier was used, so Na in-diffusion from the SLG was allowed. The ACIGS films were grown via a three-stage (group-I poor, group-I rich, group-I poor) coevaporation process, the Ag/Cu evaporation rate ratio was kept constant throughout. A higher Ga and lower In rate were applied during the initial absorber growth to facilitate the formation of a back-surface field. All ACIGS films exhibited similar GGI depth profiles and the absorber thickness varied between 2.0 and 2.4 μm. The maximum substrate temperature during the second and third stage was set to 550 °C. No alkali postdeposition treatment was applied. Integral compositions were extracted from crosscalibrated X-Ray fluorescence measurements on bare absorbers located at the outer positions of the deposition zone. After absorber formation, a 50 nm-thick CdS buffer layer was grown by chemical bath deposition. The solar cell stacks were finalized by sputtering *i*-ZnO (70 nm) and ZnO:Al (150 nm; sheet resistance $\approx 50 \Omega \square^{-1}$) on top. No antireflective coating was used for any of the cells in this study. Each sample was divided into either 16 cells (each with an area of 0.1 cm²) or 14 cells (each with an area of 0.05 cm²).

Supporting Information

Supporting Information is available from the Wiley Online Library or from the author.

Acknowledgements

The authors would like to thank Olof Stolt for fabricating the devices analyzed in this work. There are no competing interests to declare. This work was supported by the Swedish Energy Agency (48479–1) and Swedish Research Council (2019–04793).

Conflict of Interest

The authors declare no conflict of interest.

Data Availability Statement

The data that support the findings of this study are available from the corresponding author upon reasonable request.

Keywords

(Ag,Cu)(In,Ga)Se₂, Cu(In,Ga)Se₂, device stability, stoichiometry, widegap chalcopyrite, CIGS-based solar cells

Received: March 7, 2022

Revised: August 16, 2022

Published online: August 29, 2022

- [1] P. Jackson, R. Wuerz, D. Hariskos, E. Lotter, W. Witte, M. Powalla, *Phys. Status Solidi RRL* **2016**, *10*, 583.
- [2] M. Nakamura, K. Yamaguchi, Y. Kimoto, Y. Yasaki, T. Kato, H. Sugimoto, *IEEE J. Photovoltaics* **2019**, *9*, 1863.
- [3] W. Shockley, H. J. Queisser, *J. Appl. Phys.* **1961**, *32*, 510.
- [4] A. S. Brown, M. A. Green, *Physica E* **2002**, *14*, 96.
- [5] T. Leijtens, K. A. Bush, R. Prasanna, M. D. McGehee, *Nat. Energy* **2018**, *3*, 828.
- [6] M. A. Contreras, L. M. Mansfield, B. Egaas, J. Li, M. Romero, R. Noufi, E. Rudiger-Voigt, W. Mannstadt, *Prog. Photovoltaics* **2012**, *20*, 843.
- [7] P. T. Erslev, J. Lee, G. M. Hanket, W. N. Shafarman, J. D. Cohen, *Thin Solid Films* **2011**, *519* 7296.
- [8] A. Chikhalkar, M. Goryll, W. Shafarman, R. R. King, in *2019 IEEE 46th Photovoltaic Specialists Conference (PVSC)*, IEEE, Piscataway, NJ **2019**, pp. 2150–2154.
- [9] B. Huang, S. Chen, H. Deng, L. Wang, M. Contreras, R. Nou, S. Wei, *IEEE J. Photovoltaics* **2014**, *4*, 477.
- [10] J. V. Li, S. Grover, M. A. Contreras, K. Ramanathan, D. Kuciauskas, R. Noufi, *Sol. Energy Mater. Sol. Cells* **2014**, *124* 143.
- [11] T. Minemoto, T. Matsui, H. Takakura, Y. Hamakawa, T. Negami, Y. Hashimoto, T. Uenoyama, M. Kitagawa, *Sol. Energy Mater. Sol. Cells* **2001**, *67*, 83.
- [12] M. Raghuwanshi, E. Cadel, P. Pareige, S. Duguay, F. Couzinie-Devy, L. Arzel, N. Barreau, *Appl. Phys. Lett.* **2014**, *105*, 013902.
- [13] M. Raghuwanshi, R. Wuerz, O. Cojocar-Mirédin, *Adv. Funct. Mater.* **2020**, *30*, 2001046.
- [14] M. Balboul, H. Schock, S. Fayak, A. A. El-Aal, J. Werner, A. Ramadan, *Appl. Phys. A* **2008**, *92*, 557.
- [15] G. Hanna, A. Jasenek, U. Rau, H. Schock, *Thin Solid Films* **2001**, *387*, 71.
- [16] J. Pohl, K. Albe, *Phys. Rev. B: Condens. Matter Mater. Phys.* **2013**, *87*, 245203.
- [17] C. Spindler, F. Babbe, M. H. Wolter, F. Ehré, K. Santhosh, P. Hilgert, F. Werner, S. Siebentritt, *Phys. Rev. Mater.* **2019**, *3*, 090302.
- [18] J. Keller, K. V. Sopiha, O. Stolt, L. Stolt, C. Persson, J. J. Scragg, T. Törndahl, M. Edoff, *Prog. Photovoltaics* **2020**, *28*, 237.
- [19] C. Wang, D. Zhuang, M. Zhao, Y. Li, L. Dong, H. Wang, J. Wei, Q. Gong, *J. Energy Chem.* **2022**, *66*, 218.
- [20] W. Shafarman, C. Thompson, J. Boyle, G. Hanket, P. Erslev, J. David Cohen, in *2010 35th IEEE Photovoltaic Specialists Conf.*, IEEE, Piscataway, NJ **2010**, pp. 000325–000329.
- [21] T. Nishimura, A. Doi, J. Chantana, A. Mavlonov, Y. Kawano, T. Minemoto, *Sol. Energy* **2021**, *230*, 509.
- [22] H. Simchi, B. E. McCandless, K. Kim, J. H. Boyle, R. W. Birkmire, W. N. Shafarman, *IEEE J. Photovoltaics* **2012**, *2*, 519.
- [23] J. Keller, L. Stolt, K. V. Sopiha, J. K. Larsen, L. Riekehr, M. Edoff, *Sol. RRL* **2020**, *4*, 2000508.
- [24] A. Sharan, F. P. Sabino, A. Janotti, N. Gaillard, T. Ogitsu, J. B. Varley, *J. Appl. Phys.* **2020**, *127*, 065303.
- [25] J. Keller, P. Pearson, N. S. Nilsson, O. Stolt, L. Stolt, M. Edoff, *Sol. RRL* **2021**, *5*, 2100403.
- [26] M. A. Green, *Prog. Photovoltaics* **2009**, *17*, 57.
- [27] V. Fjallstrom, P. M. Salome, A. Hultqvist, M. Edoff, T. Jarmar, B. G. Aitken, K. Zhang, K. Fuller, C. K. Williams, *IEEE J. Photovoltaics* **2013**, *3*, 1090.
- [28] M. Theelen, N. Barreau, V. Hans, H. Steijvers, Z. Vroon, M. Zeman, in *2015 IEEE 42nd Photovoltaic Specialist Conf. (PVSC)*, IEEE, Piscataway, NJ **2015**, pp. 1–6.
- [29] J. F. Guillemoles, L. Kronik, D. Cahen, U. Rau, A. Jasenek, H. W. Schock, *J. Phys. Chem. B* **2000**, *104*, 4849.
- [30] G. Dagan, T. F. Ciszek, D. Cahen, *Fluid Phase Equilib.* **1992**, *96*, 3013.

- [31] J. I. Deitz, P. K. Paul, R. Farshchi, D. Poplavskyy, J. Bailey, A. R. Arehart, D. W. McComb, T. J. Grassman, *Adv. Energy Mater.* **2019**, 9, 1901612.
- [32] K. V. Sopiha, J. K. Larsen, O. Donzel-Gargand, F. Khavari, J. Keller, M. Edoff, C. Platzer-Björkman, C. Persson, J. J. Scragg, *J. Mater. Chem. A* **2020**, 8, 8740.
- [33] S. Lany, A. Zunger, *J. Appl. Phys.* **2006**, 100, 113725.
- [34] A. J. Ferguson, R. Farshchi, P. K. Paul, P. Dippo, J. Bailey, D. Poplavskyy, A. Khanam, F. Tuomisto, A. R. Arehart, D. Kuciauskas, *J. Appl. Phys.* **2020**, 127, 215702.
- [35] A. Ferguson, P. Dippo, D. Kuciauskas, R. Farshchi, J. Bailey, G. Zapalac, D. Poplavskyy, in *2018 IEEE 7th World Conf. on Photovoltaic Energy Conversion (WCPEC)*, IEEE, Piscataway, NJ **2018**, pp. 3918–3922.
- [36] A. Czudek, A. Urbaniak, A. Eslam, R. Wuerz, M. Igalson, *IEEE J. Photovoltaics* **2020**, 10, 1926.
- [37] S. Lany, A. Zunger, *Phys. Rev. Lett.* **2008**, 100, 016401.
- [38] M. Igalson, M. Maciaszek, K. Macielak, A. Czudek, M. Edoff, N. Barreau, *Thin Solid Films* **2019**, 669, 600.